High-pressure serpentinization and abiotic methane formation in metaperidotite from the Appalachian subduction, northern Vermont

(Article begins on next page)

04 May 2024

1 **High-pressure serpentinization and abiotic methanogenesis in metaperidotite from the**

2 **Appalachian subduction, northern Vermont**

3 Antoine Boutier[1,2]*, Alberto Vitale Brovarone[1,3,4], Isabelle Martinez[2], Olivier Sissmann[5], Sara

4 Mana[6]

5 [1]*Dipartimento di Scienze della Terra, Università degli Studi di Torino, Via Valperga Caluso 35,*

6 *Torino, Italy*

7 [2]*Université de Paris, Institut de physique du globe de Paris, CNRS, F-75005 Paris, France*

8 [3]*Dipartimento di Scienze Biologiche, Geologiche e Ambientali, Alma Mater Studiorum*

9 *Università di Bologna. Piazza di Porta San Donato 1, Bologna, Italy*

10 [4]*Institut de Minéralogie, de Physique des Matériaux et de Cosmochimie (IMPMC), Sorbonne*

11 *Université, Muséum National d'Histoire Naturelle, UMR CNRS 7590, IRD UR206, 75005 Paris,*

12 *France*

13 [5]*IFP Energies Nouvelles, 92500 Rueil-Malmaison, France*

14 [6]*Department of Geological Sciences, Salem State University, Salem, MA 01970, USA*

15 *Corresponding author: antoine.boutier@unito.it

1   **Abstract**

2   Serpentinization is the process of hydroxylation of olivine-rich ultramafic rocks to produce

3   minerals such as serpentine, brucite and magnetite. This process is commonly accompanied

4   by Fe oxidation and release of H_2, which can be involved in abiotic reaction pathways leading

5   to the genesis of abiotic light hydrocarbons such as methane (CH_4). Examples of this

6   phenomenon exist at the seafloor, such as at the serpentinite-hosted Lost City hydrothermal

7   field, and on land in ophiolites at relatively shallow depths. However, the possibility for

8   serpentinization to occur at greater depths, especially in subduction zones, raises new

9   questions on the genesis of abiotic hydrocarbons at convergent margin and its impact on the

10   deep carbon cycle. High-pressure ultramafic bodies exhumed in metamorphic belts can

11   provide insights on the mechanisms of high-pressure serpentinization in subduction zones

12   and on the chemistry of the resulting fluids. This study focuses on the ultramafic Belvidere

13   Mountain complex belonging to the Appalachian belt of northern Vermont, USA.

14   Microstructures show overgrowth of both primary (Mg# 0.91) and metamorphic (Mg# 0.95)

15   olivine by delicate antigorite crystals, pointing to at least one stage of serpentinization at high-

16   temperature conditions and consistent with the high-pressure subduction evolution of the

17   Belvidere Mountain complex. Formation of ubiquitous magnetite and local Fe-Ni alloys

18   testifies to the partial oxidation of Fe^{2+} into Fe^{3+} and generation of reduced conditions. Fluid

19   inclusion trails cross-cutting the primary olivine relicts suggest their formation during the

20   antigorite serpentinization event. MicroRaman spectroscopy on the fluid inclusions reveals a

21   CH_4-rich gaseous composition, as well as N_2, NH_3 and H_2S. Moreover, the precipitation of

22   daughter minerals such as lizardite and brucite in the fluid inclusions indicate the initial

23   presence of H_2O in the fluid. High-pressure serpentinization driven by the infiltration of

24   metasediment-derived aqueous fluids is proposed at the origin of CH_4 and other reduced fluid

25   species preserved in the fluid inclusions. This suggests the Belvidere Mountain complex as an

26   example of deep abiotic hydrocarbon genesis related to high-pressure serpentinization in an

27   early Paleozoic subduction zone.

1   Introduction

2   Alteration of ultramafic rocks by aqueous fluids, or serpentinization, produces serpentine-rich

3   rocks and may be accompanied by redox reactions leading to the formation of H_2 and abiotic

4   light hydrocarbons (Mével, 2003; Moody, 1976; Seyfried Jr et al., 2007). Oxidation of Fe^{2+} in

5   mantle minerals and formation of Fe^{3+} minerals such as magnetite produces H_2, which may

6   then promote the conversions of dissolved carbon-bearing species into abiotic CH_4 (Andreani

7   et al., 2013; Berndt et al., 1996). Serpentinization is well documented at mid-ocean ridges and

8   on land (Andréani et al., 2007; Cannat et al., 2010; Etiope et al., 2011; Klein et al., 2014;

9   Schrenk et al., 2013), where H_2 and CH_4 produced through serpentinization can support

10   biological communities and could be linked to the emergence of early life on Earth (Kelley et

11   al., 2005; Ménez et al., 2018; Sleep and Bird, 2007). Serpentinization processes may also

12   happen at much greater depths and affect subducted mantle sections and the overlying

13   mantle wedge at convergent margins (Guillot et al., 2015, 2000; Vitale Brovarone et al., 2017;

14   Wada et al., 2008), owing to the availability of aqueous fluids (Bebout and Penniston-Dorland,

15   2016; Deschamps et al., 2013). However, the patterns of serpentinization reactions at high-

16   temperature (HT) and high-pressure (HP) conditions, here defined with respect to the

17   serpentine stability field, and the associated fluid-rock redox budgets are still largely

18   unconstrained. The possibility that HT-HP serpentinization may not involve Fe oxidation and

19   genesis of H_2 has been proposed (Evans, 2010). However, natural case studies of slab-derived

20   serpentinized peridotites suggest that magnetite, H_2 and abiotic CH_4 can be produced at these

21   conditions (Vitale Brovarone et al., 2020). Ultramafic bodies in metamorphic belts can provide

22   good insights on the mechanisms of HP-HT serpentinization and the resulting fluids (Evans et

23   al., 2017), and therefore make good case studies for the investigation of the mechanisms of

24   serpentinization in subduction zones.

25   The Belvidere ultramafic complex, Vermont, USA, is a fragment of the Iapetus ocean that was

26   involved in the Taconic orogeny and recorded HP metamorphism during Cambrian-Ordovician

27   (Chew and van Staal, 2014; Gale, 1980; Honsberger et al., 2017). This complex includes

28   variably serpentinized peridotites bearing antigorite, the HT serpentine polysome stable at

29   subduction zone HP conditions (Schwartz et al., 2013), therefore making a potential example

30   of HT-HP serpentinization. In this work, we integrate field, microstructural, thermodynamic,

31   and fluid inclusions data to investigate the patterns and timing of serpentinization of the

32   Belvidere ultramafic complex, with particular focus on the HP fluid-rock interactions recorded

33   by these rocks.

34   **1. Geologic setting**

35   The Belvidere Mountain complex (BMC) area is part of a North-South trending belt of

36   mafic/ultramafic rocks belonging to the Appalachian Mountain system and extending form

37   Newfoundland to Georgia (Gale, 2007; Hibbard et al., 2006)(Fig. 1). These ultramafic bodies

38   mainly consist of variably serpentinized peridotites, and associated metabasic and metafelsic

39   rocks   tectonically   embedded   within   Cambrio-Ordovician   metasedimentary   and

40   metavolcanics formations (Chidester et al., 1978; Gale, 1986, 1980; Laird et al., 1984; Van

41   Baalen et al., 2009). The BMC, as well as other mafic/ultramafic complexes such as the

42   Tillotson Peak and the Pennington complexes, are interpreted to represent remnants of an

43   ocean-continent transition zone associated with the extension of the Laurentian margin

44   (Chew and van Staal, 2014). These terranes were successively involved in the closure of the

45   Iapetus Ocean during the Ordovican Taconic orogeny (Doolan et al., 1982; Honsberger et al.,

46   2017; Karabinos et al., 1998; Laird et al., 1984; Stanley et al., 1984). The BMC forms a 6.5 km

47   long body that structurally overlies the metasedimentary Ottauquechee and Stowe

48   Formations to the East and is overlain by the Hazen Notch formation to the West. The Stowe

49   Formation is late Cambrian, composed of gray-green quartz -chlorite-sericite +/- magnetite

50   schists. The Ottauquechee Formation is middle Cambrian consisting carbonaceous

51   pyritiferous phyllite. The Hazen Notch Formation is dated from Neoproterozoic to Cambrian,

52   graphitic and non-graphitic quartz-albite-sclerite-chlorite schist, along medium-grained,

53   massive, quartz-albite-muscovite gneiss. The internal architecture of the BMC comprises,

54   from top to bottom, variably serpentinized dunite and harzburgite, coarse-grained and fine-

55   grained amphibolite, greenstone, muscovite schist, and albite gneiss (Gale, 1986, 1980; Van

56   Baalen et al., 2009). Lenticular bodies composed of talc-carbonate rocks and steatite, often

57   including cores of relatively unserpentinized peridotite, are observed within the BMC, and

58   range size from a few meters to several tens of meter (Chidester et al., 1978). The BMC rocks

59   underwent Taconic blueschist-facies peak metamorphic conditions constrained at 0.9-1.3 GPa

60   and 510-520 °C in metabasic rocks (Honsberger, 2015; Laird et al., 1993). Slightly higher P,

61   blueschist-to-eclogite-facies metamorphic conditions are recorded by the Tilliston Peak mafic

62   rocks located just north of the BMC (Laird et al., 1993, 1984). This tectonometamorphic event

63   has been dated at 505-473 Ma by $^{40/39}$Ar amphibole and mica geochronology (Castonguay et

64   al., 2012; Laird et al., 1993).

65   **2. Methods**

66   Quantitative energy-dispersive X-ray spectroscopy (EDS) analyses and backscattered electron

67   (BSE) imaging were carried out using the JSM-IT300LV Scanning Electron Microscope Oxford

68 Inca Energy Dispersive Spectrometer at the Department of Earth Sciences of Turin University.

69 Data were processed with the INCA software from Oxford Instruments. Quantitative analysis

70 employed 15kV accelerating voltage and 20 s to 40 s counting time. Natural and synthetic

71 mineral and oxide standards were employed. EDS calibration was made using Cobalt

72 standard.

73 Quantitative wavelength-dispersive spectrometer (WDS) analyses were carried out using a

74 JEOL 8200 Super Probe at the Department of Earth Sciences "Ardito Desio" of Milan

75 University. The microprobe was using a 15keV accelerating voltage under 5 nÅ, with 30s

76 counting time under maximum emission peak. Sixteen oxide composition were measured,

77 using synthetic and natural standards: grossular (Si, Al and Ca), omphacite (Na), K-feldspath

78 (K), fayalite (Fe), forsterite (Mg), rhodonites (Mn), niccolite (Ni), ilmenite (Ti), galena (Pb and

79 S), pure Cr, pure Zn and pure Cu.

80 MicroRaman spectroscopy of minerals and fluid inclusions was done at the Department of

81 Earth Sciences, University of Turin, with a LabRAM HR (VIS) (HORIBA Jobin Yvon) equipped of

82 a 532.11 nm, solid-state Nd laser, a Super Notch Plus filter with spectral resolution of 1 cm−1,

83 and a grating of 600 grooves/mm. The laser of emission power was set at 80 mW and focused

84 to 5 μm with a ×100 objective with a laser power on the sample < 5 mW. Calibration was

85 performed using the 520.6 cm−1 band of a silicon standard for the 100-2000 cm^{-1} range, and

86 the 2331 cm-1 band of atmospheric N_2 for the 2000-4000 cm^{-1} range. Four accumulations of

87 30–60 s were collected for each spectrum. Raman spectra of fluid inclusions were performed

88 on double-polished thick sections unless otherwise specified.

89   Isotopic composition measurements of methane were performed on a MAT 253 (Thermo

90   Fisher) mass spectrometer, coupled with gas chromatography (GCC-IR-MS) in order to purify

91   the samples. The gas phase was extracted and measured after crushing the rock sampler

92   under vacuum.

93   Thermodynamic modelling was performed using the Deep Earth Water (DEW) Model

94   (Sverjensky et al., 2014) and the EQ3/EQ6 software (Wolery and Jarek, 2003) with a modified

95   Berman database (Berman, 1988). EQ3 was used to calculate the composition of a fluid in

96   equilibrium with a given mineral assemblage as, fO_2, P and T. EQ6 was used to model the

97   interaction of fluid compositions from EQ3 with another mineral assemblage as function of

98   the fluid/rock (F/R) ratio.

99   **3. Sample description and mineral chemistry**

100   In this section, we present the petrography, microstructures and mineral chemistry of

101   samples collected in the Belvidere mine (Fig. 2) and showing different degrees of

102   serpentinization. The selected samples range from weakly serpentinized dunite (V18-2a and

103   V18-2b) to partially serpentinized dunite including layers of boudinaged meta-pyroxenite

104   (V18-3a and V18-3b), to fully serpentinized peridotite (V18-B3).

105   **3.1. *Microstructural characterization***

106   Sample V18-2a (least serpentinized dunite) consists of olivine (~80 vol.%), antigorite (~10

107   vol.%), Cr-spinel (>5 vol.%), magnetite (<5 vol.%), chlorite (<1 vol.%), sulphides (<1 vol.%), and

108   alloys (<1 vol.%) determined from visual estimate in thin section. Primary olivine forms

109   crystals ranging in size from 0.25 to 1 mm (Fig. 3A). It is partially replaced by antigorite, as

110   identified by MicroRaman spectroscopy (Fig. 4), along mesh-like structures (Fig. 3A-C).

111   Antigorite is present as elongated crystals, up to 200 μm in length, which statistically

112   overgrew the olivine (Fig. 3C). Magnetite is present in three microstructural domains: as large,

113   millimeter scale crystals rimming chromite relicts, as grains of ~50 μm in the mesh structures,

114   and as millimeter scale crystals in antigorite veins. Chlorite is found, together with magnetite,

115   around Cr-spinel relicts (Fig. 3B).

116   Sample V18-2b (serpentinized dunite) consists of antigorite (~40 vol.%), olivine (~40 vol.%,

117   including primary and metamorphic olivine), magnetite (>5 vol.%), chlorite (>5 vol.%), brucite

118   (<5 vol.%), and alloys (<1 vol.%). The structure is similar to V18-2a, but in this case the extent

119   of serpentinization along the meshes is higher. SEM backscattered-electron imaging reveals

120   the presence of a second generation of olivine, hereafter metamorphic olivine (see Section

121   4.2 for discussion) growing in two different sites: epitaxially on the primary olivine and

122   replacing former orthopyroxene (Fig. 5A-B). Striped zoning is observed in primary olivine (Fig

123   5A), as described in Plümper et al., 2012a, alternating thin forsterite-richer and forsterite-

124   poorer olivine composition. The initial presence of orthopyroxene in the rock is inferred based

125   on the presence of clinopyroxene exsolutions preserved in metamorphic olivine-rich

126   pseudomorphoses (Fig. 3D and 5B). Antigorite is present as elongated (0.5 mm in length)

127   crystals and as fine-grained aggregates in the matrix. The elongated antigorite crystals are

128   chemically zoned, with bright core and dark rim in backscattered electron imaging (Fig. 5A).

129   Raman spectra of both generations exhibit the characteristic 1043 cm^{-1} band of antigorite,

130   whereas the main OH stretching is at 3664 cm^{-1} in the bright core and at 3673 cm^{-1} in the dark

131   rim (Fig 4C), both inconsistent with antigorite-lizardite mixing. The higher Raman shift of the

132   dark rim may be linked to variation of pressure condition (Auzende et al., 2004). The dark

133 antigorite generation appears the same forming the fine-grained aggregates. The bright

134 antigorite generation (at the core of large crystals) is never found in contact with either

135 primary or metamorphic olivine, whereas the darker antigorite generation (at the rim of large

136 crystals of disseminated in the matrix) is in contact with them (Fig. 5A). Magnetite is more

137 abundant relative to sample V18-2a, especially along meshes. Brucite was identified by SEM

138 and Raman (Fig. 4D) in veins, sometimes associated with metamorphic olivine (Fig. 5C). Alloys

139 and sulphides are present in association with antigorite and are locally associated to

140 magnetite (Fig. 5D).

141 Samples V18-3a and 3b are from a boudinaged layer of clinopyroxenite included in an

142 intensely serpentinized dunite (Fig. 3E-G). The mineral assemblage and microstructures of the

143 serpentinized dunite part of the sample is similar to sample V18-2b, yet more intensely

144 serpentinized. The primary clinopyroxene is fully replaced by diopside aggregates in both the

145 clinopyroxenite layer and the host dunite. The primary clinopyroxene sites in this sample are

146 slightly different from the serpentinized dunite, with less abundant magnetite and

147 characteristic fan-shaped diopside aggregates in the former compared to the latter.

148 Metamorphic olivine is present at the rim of primary clinopyroxene and along its cleavages,

149 together with antigorite (Fig. 5E-F). In the latter case, metamorphic olivine is localized along

150 thin arrays encircled by antigorite (Fig. 5F). Antigorite shows the same chemical zoning as

151 observed in the dunite, with brighter cores and darker rims in backscatter electron imaging

152 (Fig. 5G). Backscattered electron imaging reveals that the dark antigorite shows similar

153 overgrowth microstructural relationships with both primary and metamorphic olivine (Fig.

154 5E). The microstructures reflect either equilibrium between antigorite and the two olivine

155 generations, or overgrowth of both olivine generations by the antigorite. Considering that the

156   amount of primary olivine strongly decreases in favour of antigorite in several samples, which

157   suggests serpentinization of the primary olivine, second antigorite generation formed after

158   the growth of metamorphic olivine appears . It is possible, even though the microstructures

159   could not confirm it, that the first antigorite generation grew prior to or together with the

160   metamorphic olivine. Magnetite is present in four different structural sites: as arrays of ~50

161   μm size crystals along the meshes, as trails of ~50 μm crystals in primary olivine and

162   clinopyroxene pseudomorphoses, as aggregates rimming the primary Cr-spinel, and as

163   millimeter scale aggregates along discordant veins. The Cr-spinel sites are characterized by

164   three different layers: a rather preserved core, a mantle of ferritchromite, and a rim of

165   magnetite (Fig. 5E; see Section 4.2).

166   Sample V18-B3 is a fully serpentinized peridotite. The matrix is composed of a mixture of

167   antigorite and chrysotile (identified by MicroRaman) with magnetite. Brucite is observed

168   replacing pyroxene sites and is associated with magnetite and/or metamorphic olivine (Fig.

169   3H and 5H). Based on the microstructural observations on sample V18-2b, these

170   pseudomorphoses are interpreted as former orthopyroxene crystals replaced by

171   metamorphic olivine and successively hydrated to form serpentine + brucite ± magnetite.

172   **3.2. Mineral chemistry**

173   Primary olivine has Mg# of 0.91-0.92 [Mg# = Mg/(Fe+Mg)], whereas metamorphic olivine is

174   enriched in Mg (Mg# of 0.95) (Table 1, Fig. 6). The Mn# [Mn# = Mn/(Mn+Fe+Mn+Ni)] of

175   metamorphic olivine (0.0040 ±0.0006) is much higher than primary olivine (0.0015 ±0.0005).

176   Metamorphic olivine analyses in sample V18-B3 show slightly lower Mg# and higher Mn#

177   content relative to metamorphic olivine from other samples. Metamorphic olivine rimming

178 the primary orthopyroxene sites in sample V18-3a has higher CaO content (0.25 wt.%)

179 compared to the metamorphic olivine overgrowing primary olivine in V18-2b (0.02 wt.%).

180 Metamorphic olivine in the sample V18-B3 show slightly lower Mg# and highly increased MnO

181 content (1.2 wt %) in regard to metamorphic olivine from other samples. The NiO content of

182 primary olivine (0.38 to 0.49 wt.%) and metamorphic olivine (0.39 to 0.46 wt.%) are similar.

183 The incorporation of Mn in olivine appears to be characteristic of metamorphic olivine from

184 several localities regardless of the olivine formation environments (dehydration vs.

185 hydration). The Mg# of metamorphic olivine relative to primary olivine may depend upon

186 several parameters such as the stability of different Fe-bearing minerals, the Fe partitioning

187 among them, and the P-T and redox conditions (Frost and Beard, 2007; Majumdar et al., 2016;

188 Nozaka, 2018, 2003). An increase in Mg# (and MnO) in metamorphic olivine relative to

189 primary olivine has been observed in inferred mantle wedge peridotites recording HP

190 serpentinization (Dandar et al., 2019; Guillot et al., 2000). Plümper et al., 2012a report striped

191 Mg# zoning in hydrated supra-subduction mantle rocks as the result of chemical interaction

192 during antigorite serpentinization at high temperature conditions. Metamorphic olivine

193 formed through prograde antigorite + brucite dehydration shows either lower or higher Mg#

194 compared to mantle olivine (Arai et al., 2012; Debret et al., 2013; Iyer et al., 2008; Kempf and

195 Hermann, 2018; Nozaka, 2018; Plümper et al., 2012b; Scambelluri et al., 1995; Shen et al.,

196 2015)(Fig. 6).

197 The core of individual, elongated antigorite crystals exhibits higher FeO (1.6 to 2.6 wt.% [Mg#

198 0.94-0.96]), Al_2O_3 (1.77 wt.%) [Mg# =Mg/(Mg+ΣFe)], and Cr_2O_3 (0.61 wt.%) than the rim (1.35

199 wt.% [Mg# 0.97], 0.52 wt.%, 0.13 wt.%, respectively) (Table 1). Unzoned matrix antigorite has

200   a composition equivalent to the rim of the elongated antigorite crystals. The Mn# [Mn# =

201   Mn/(Mn+Fe+Mn+Ni)] of antigorite is 0.0006 (±0.0004).

202   The preserved spinel core has Cr# [Cr/(Cr+Al)] of 0.79 (Table 2). The mantle overgrowing the

203   primary spinel has a ferritchromite mantle of Cr-magnetite with a Cr# of 0.91 and higher MnO

204   relative to the core. The magnetite rims with no Al_2O_3, but high Cr_2O_3 (1.87 wt.%). The

205   composition of magnetite in the meshes and veins differs from magnetite found in the spinel

206   sites, with very little Cr_2O_3.

207   Diopside has a Mg number [Mg# =Mg/(Mg+Fe)] of 0.98. Chlorite has an Mg# [Mg#

208   =Mg/(Mg+ΣFe)] of 0.95, and Cr_2O_3 up to 4.07 wt.% (Table 1).

209   Brucite has up to 3 wt.% FeO (as total Fe), Mg# [Mg# =Mg/(Mg+Fe)] of 0.97 (Table 2). Alloys

210   and sulfides are Ni rich, with various amounts of S, Fe and trace amounts of Pb, Cu, et Co

211   (Table 3). Alloys mainly consist of Cu-bearing FeNi alloy (taenite) (Table 3). Sulphides include

212   Ni, Cu, and Fe sulphides. Only heazlewoodite (NiS) was analysed whereas for other sulphides

213   proper analyses could not be obtain owing to the small grain sizes.

214   **3.3. Fluid inclusion analysis**

215   Primary olivine in all samples is rich in fluid inclusions forming secondary trails (Fig. 7). The

216   fluid inclusion trails are confined within individual crystals and show two alternative structural

217   relationships relative to the antigorite veins, being either cut by them (Fig. 7A) or injected

218   from them (Fig. 7B-C). These patterns suggest a secondary fluid trapping during the antigorite

219   serpentinization event forming the main mesh structure observed in the rock.

220   Fluid inclusions exhibit rounded to elongated shapes (Fig. 7D-E). Optical microscope

221   observations at room conditions suggest that the fluid inclusions are either single-phase and

222   gaseous, or bi-phase with solid and gas. MicroRaman spectra of fluid inclusions are presented

223   in Fig. 8. The spectra show the presence of marked CH_4 bands (2912 cm^{-1}), as well as N_2 (2327

224   cm^{-1}), NH_3 (3324 cm^{-1}), S-H/H_2S (2575 cm^{-1}). Free H_2O in the fluid inclusions was not detected

225   by MicroRaman. However, the presence of tiny amounts of free H_2O in the fluid inclusions —

226   undetectable by MicroRaman at room conditions— cannot be excluded (Berkesi et al., 2009;

227   Lamadrid et al., 2017).

228   The molar fraction of gas in the gas mixture was estimated using the Raman scattering cross-

229   section and the instrumental efficiency of each species. Using equation presented in Frezzotti

230   *et al.*, 2012, we obtain the following molar proportion: CH_4 = 92±6%, N_2 = 6±5%, H_2S = 1±1%

231   and NH_3 = 1±2% for the mean composition of twenty inclusions in olivine from all samples (Fig

232   9). Composition within the same inclusion trail show molar fractionation variation smaller

233   than 1% but different trail within the same crystal can exhibit up to 10% of molar fraction of

234   CH_4 and could reflect fluid heterogeneity. Alternatively, this effect can be the result of

235   different crystal orientation during data acquisition (Caumon et al., 2019). No clear pattern

236   was observed linked to relationship between inclusion trails and antigorite veinlets.

237   Solid phases were identified in large fluid inclusions. MicroRaman analysis revealed the

238   presence of lizardite and brucite but no magnetite was detected. Some inclusions contain

239   graphite as a solid phase in the inclusion in addition (Fig. 7F and Fig. 8B). The only sporadic

240   presence of graphite in the fluid inclusions, and in particular in inclusions resulting from

241   necking processes, suggest that this mineral precipitated as a result of local respeciation of

242   the fluid inclusions (Cesare, 1995). The presence of hydrous phases is the inclusions suggests

243 re-equilibration of the inclusion with the host mineral, effectively serpentinizing the olivine

244 and consuming water initially present in the inclusions. However, the presence of step-

245 daughter minerals in the inclusion is not systematic, suggesting that the initial fluid was

246 already rich in CH_4 (-N_2-NH_3-H_2S) at the time of trapping, and that the reduced fluid species

247 did not form only inside the fluid inclusions.

248 **3.4. Rodingite**

249 Rodingite are ultramafic rocks that are composed of carbonate, garnet, diopside, epidote ±

250 graphite. While not being the focus of this study, the carbonate in the rodingite bear

251 numerous trails of fluid inclusions. Fluid inclusions exhibit negative crystal shape and are

252 single-phase gaseous. The composition of the carbonate-hosted fluid inclusions, as revealed

253 by Raman spectroscopy, is essentially CH_4 and N_2. Using quantitative estimation of inclusions

254 in carbonates (see section 4.3) yield molar fractions of $N_2 = 67±4\%$, $CH_4 = 33±4\%$ on four

255 different inclusions.

256 **3.5. Thermodynamic modelling**

257 Thermodynamic calculations were performed in order to constrain the mineralogical, fluid

258 and redox pattern of the HP serpentinization. Because the selected partially serpentinized

259 samples are comprised in strongly serpentinized rocks and embedded in metasediment, two

260 fluid equilibriums can be considered. For silica-rich fluid sources (e.g. metasedimentary rocks

261 or talc-bearing ultramafic rocks), the predicted assemblages do not match the natural

262 samples. For this reason, the fluid composition calculated with EQ3 was equilibrated with a

263 serpentinite consisting of antigorite + magnetite + brucite + chlorite + olivine. This fluid then

264 reacted with a dunite with mineral modal proportions comparable with the study samples

265 and consisting of 92% olivine (forsterite 90%, fayalite 10%), 5.4% orthopyroxene (enstatite

266 90%, ferrosilite 10%), 2.5% clinopyroxene (diopside 90%, hedenbergite 10%) and 0.1% spinel.

267 The fO_2 of the infiltrating fluid was set at the quartz-fayalite-magnetite (QFM) buffer. The

268 calculations were done at temperatures consistent with the peak metamorphic conditions

269 estimated for the BMC, i.e., 400 °C to 500 °C and 1 GPa (Honsberger, 2015; Laird et al., 1993),

270 and for different F/R ratios. Figure 10 shows the mineralogical evolution as a function of

271 reaction progress at 450 °C and 1GPa for a fluid rock ratio of 1. The model reaction proceeds

272 with progressive transformation of, from the first to the last reacting mineral, mantle spinel,

273 clinopyroxene, orthopyroxene, and olivine. Magnetite starts to form during the early stages

274 of the reaction along with chlorite in response to spinel consumption. Reaction of mantle

275 pyroxenes marks the precipitation of metamorphic clinopyroxene (diopside 93%,

276 hedenbergite 3.35% and clino-enstatite 3.65%), metamorphic olivine, antigorite, and

277 additional magnetite. The late formation of antigorite marks the partial consumption of

278 metamorphic olivine and a decrease in its Mg#, from Mg# 0.90 to Mg# 0.83. These patterns

279 reflect the microstructural features observed in the natural samples. For example, spinel

280 appears intensely replaced by chlorite in rather unserpentinized portions of the rock (Fig.

281 10A). Similarly, mantle olivine adjacent to fully replaced mantle pyroxenes is commonly little

282 affected by the serpentinization. Both mantle and metamorphic olivine in the natural samples

283 appear texturally replaced by antigorite, as also suggested by the modelling while

284 approaching equilibration. With the chosen bulk composition and used thermodynamic data

285 set, the formation of antigorite is limited to T < 470 °C. The antigorite stability field could be

286 enlarged by considering iron in the antigorite thermodynamic model. The fO_2 decreases

287 progressively during the reaction progress, with a steep decrease during the formation of

288 antigorite down to ΔLog QFM = -1.2 (Fig. 10C). Methane, initially about 1 order of magnitude

289 less concentrated than CO_2 in the reacting fluid, becomes a dominant species at reaction

290 completion (about 1 order of magnitude more concentrated than CO_2). Nevertheless,

291 variations of parameters such as F/R ratio, mineralogy, or temperature, were found to affect

292 the proportion of CH_4 and CO_2. As an example, increasing the modal proportion of either

293 orthopyroxene or clinopyroxene in the initial rock or decreasing the F/R ratio appears to

294 favour a higher proportion of CH_4 in the fluid in respect to CO_2. The model predicts high

295 relative concentration of H_2 in the fluids, however H_2 was not detected in natural samples by

296 micro-Raman spectroscopy. Sulphur and nitrogen speciation were also assessed, with HS^- and

297 H_2S and NH_3 being the dominant sulphur species relative to HSO_4^- and N_2 and NH_4^+,

298 respectively (Fig. 10B).

4. Discussion

4.1. Patterns and timing of serpentinization

301 The timing of serpentinization of slab-derived, exhumed HP serpentinized rocks can span

302 (sub)seafloor conditions prior to subduction, prograde hydration during subduction, or

303 retrograde hydration during exhumation. The BMC complex has been interpreted as a

304 fragment of subducted Iapetus lithosphere, and therefore may have recorded different stages

305 of serpentinization. Although the possibility of at least some (sub)seafloor serpentinization

306 prior to the Taconic subduction cannot be excluded, our data cannot provide any proof of

307 such a pre-subduction event and, instead, suggest a main hydration event at HP-HT conditions

308 in the subduction zone.

309 Besides late chrysotile veinlets, antigorite is the only serpentine polysome identified in the

310 BMC rocks. Although formation of antigorite may occur in a wide range or P-T conditions also

311 as a function of chemical parameters such as the silica activity (Rouméjon et al., 2019),

312   serpentinites dominated by antigorite are generally referred to the HT temperature part of

313   the serpentine stability field, generally above ~300-400 °C (Evans, 2004; Schwartz et al.,

314   2013). In most subduction zone settings, these conditions also correspond to relatively HP

315   conditions above 1 GPa. However, the presence of antigorite does not necessarily imply the

316   serpentinization event to have happened at HP-HT conditions because it could also have

317   formed as a result of the prograde transformation of lizardite or chrysotile following the

318   reaction:

319   17 Lizardite/Chrysotile = Antigorite + 3 Brucite   (1)
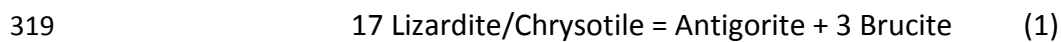
320   Nevertheless, several lines of evidence indicate that the BMC rocks recorded a stage of HP-

321   HT serpentinization. As a first general consideration, the presence of fresh mantle

322   assemblages throughout the complex (Chidester *et al.*, 1978; this study) represents a suitable

323   condition to promote HP-HT serpentinization in the subduction zone, if aqueous fluids are

324   available. Such a process has already been proposed in other HP ultramafic massifs preserving

325   fresh mantle assemblages (e.g. Früh-Green et al., 2004; Scambelluri and Tonarini, 2012; Vitale

326   Brovarone et al., 2020, 2017). The BMC rocks provides evidence for such a HP hydration event.

327   Figure 11 summarizes the proposed fluid-rock evolution of the BMC rocks as inferred from

328   the studied samples. The first indication of serpentinization (stage I in Fig. 11) is suggested by

329   the growth of elongated metamorphic olivine on the primary clinopyroxene sites (Fig. 5G),

330   which suggests the former presence of serpentine blades overgrowing the primary

331   clinopyroxene. The selective growth of serpentine at the expense of clinopyroxene rather

332   than primary olivine places this hypothetical event at HT conditions (Klein et al., 2013) and

333   possibly in the antigorite stability field (Fig. 12). Metamorphic olivine is most commonly

334   interpreted to form in response of serpentine dehydration during prograde metamorphism

335 (Plümper et al., 2017; Scambelluri et al., 1991). Figure 12 provides a compilation of traditional

336 serpentine dehydration reactions leading to the formation of metamorphic olivine. The peak

337 metamorphic conditions proposed for the BMC (0.9-1.3 GPa and 520 °C) are consistent with

338 the first olivine-forming reaction involving antigorite + brucite as reactants. Moreover, several

339 studies have shown that olivine can form at T conditions lower than the reactions shown in

340 figure 12 as a result of local bulk compositional features (Plümper et al., 2017). Alternatively,

341 metamorphic olivine after orthopyroxene may also have formed in response to hydration

342 rather than dehydration reactions, as already proposed for serpentinized mantle wedge rocks

343 (Dandar et al., 2019) following the reaction:

344 Orthopyroxene + 0.46 Water + 0.35 Mg^{2+}=

345 $\qquad\qquad\qquad\qquad$ 0.59 M-olivine +0.06 Antigorite + 0.29 Silica + 0.7 H^+ (2)

346 Followed by the hydration of olivine to form antigorite following the reaction

347 $\qquad\qquad$ Olivine + 1.29 Water + 0.42 Silica = 0.71 Antigorite   (3)

348 In either case (hydration or dehydration), the amount of serpentinization predating the

349 formation of metamorphic olivine must have been very low and, if any, related to a HT event.

350 The second, more robustly constrained stage of transformation (stage II in Fig. 11) is

351 characterized by the formation of metamorphic olivine after primary orthopyroxene, and as

352 rim around primary clinopyroxene (now recrystallized into diopside). This reaction was

353 observed in rocks containing rather undisturbed primary olivine, which again point to HT

354 serpentinization conditions (Klein et al., 2013). The partial preservation of clinopyroxene

355 exsolution lamellae inside metamorphic olivine pseudomorphic on orthopyroxene may

356 suggest nearly isovolumetric replacement during this event (Plümper et al., 2012b; Viti et al.,

357 2005). The thermodynamic modeling results suggest that, at 450 °C and 1 GPa, a transient

358 antigorite generation may have formed together with metamorphic olivine early in the fluid-

359 rock interaction, along with spinel breakdown. The Al-Cr-rich antigorite cores (Atg1) observed

360 in the studied samples may testify to this transient antigorite formation. The application of

361 empirical distribution coefficient K_D for antigorite and olivine by Evans, 2008 and

362 Trommsdorff and Evans, 1974 support this hypothesis (Table 4). The empirical Mg distribution

363 coefficient K_D [antigorite/olivine, $K_D = (\sum Fe/Mg_{Srp})/(Fe/Mg_{Ol})$] proposed by Evans, 2008 is 0.45-

364 0.35 upon consideration of ferric iron in the antigorite. The Atg1/metamorphic olivine

365 apparent K_D is 0.49-0.25, which agrees with the value proposed by Evans, 2008 for

366 equilibrium, compared with other antigorite/olivine pairs (Atg1/primary olivine = 0.14-0.25;

367 matrix antigorite (Atg2)/primary olivine = 0.11; Atg2/metamorphic olivine = 0.17-0.25). The

368 Mn distribution between antigorite and olivine gives similar results. The empirical Mn

369 distribution coefficients for antigorite/olivine equilibria is 0.18 (Trommsdorff and Evans,

370 1974). The Atg1/metamorphic olivine pair has apparent appears K_D of 0.14-0.18, thus

371 consistent with the predicted equilibrium (Table 4).

372 The third stage (stage III in Fig. 11) is characterized by the growth of a matrix antigorite (Atg2)

373 at the expense of both primary and metamorphic olivine. This event may mark either

374 retrograde hydration along the exhumation path of the BMC, or the progression of the fluid-

375 rock interaction. As indicated by the thermodynamic modeling results, a second antigorite

376 generation is expected to form at 450 °C and 1 GPa after the precipitation of metamorphic

377 olivine (Fig. 10A). The modeling predicts this second antigorite and metamorphic olivine to be

378 stable together. However, the apparent K_D for matrix antigorite and metamorphic olivine

379 suggest disequilibrium (equilibrium Mg K_D = 0.45, measured = 0.17-0.25; equilibrium Mn K_D =

380   0.18, measured = 0.09-0.14) (Table 4). This feature suggests that stage III marks the beginning

381   of retrograde hydration.

382   The fourth stage of serpentinization (IV in Fig. 11) is characterized by the complete

383   serpentinization of primary olivine and partial to full serpentinization of metamorphic olivine.

384   The partial preservation of metamorphic olivine after orthopyroxene in sample free of any

385   primary olivine relict indicates that the largest event of serpentinization of the BMC rocks

386   took place after the formation of metamorphic olivine. The presence of both antigorite and

387   lizardite + brucite at the expense of metamorphic olivine after orthopyroxene suggests that

388   this event protracted during the cooling of the BMC metamorphic path to temperatures lower

389   than 400 °C (Fig. 12).

390   In summary, based on the collected petrographic and thermodynamic data, the dominant

391   serpentinization event observed in the BMC complex is interpreted to have taken place in the

392   Taconic subduction zone.

393

394   **4.2. Timing of fluid inclusion formation and origin of CH$_4$**

395   **4.2.1. Timing of fluid inclusion entrapment**

396   Fluid inclusions in the BMC ultramafic and related metasomatic rocks contain reduced fluid

397   species such as CH$_4$, NH$_3$, and H$_2$S. The timing of fluid inclusion formation, as well as the origin

398   of their reduced speciation, is discussed in this section.

399   Reduced fluids have been found to form in ultramafic systems in a wide range of geologic

400   conditions spanning mid-ocean ridges, obducted ophiolitic massifs, and orogenic peridotite

401   bodies, in subduction, and in the upper mantle (Andréani et al., 2007; Etiope et al., 2011;

402   Schrenk et al., 2013). In the BMC rocks, the fluid inclusions may have formed in three different

403   stages of the evolution of the massif and corresponding to three different geodynamic

404   settings: (i) in the mantle prior to the formation of the Iapetus Ocean, (ii) during the

405   (sub)seafloor evolution prior to subduction, and (iii) in the subduction zone.

406   A primary mantle origin can be ruled out because the observed fluid inclusions occur as

407   secondary trails propagating from the antigorite veinlets crossing olivine crystal. A

408   (sub)seafloor origin would match the identification of CH_4-rich fluid inclusions in oceanic

409   peridotite (Cannat et al., 2010; Holm and Charlou, 2001). However, in this case, the fluid

410   inclusions would have been preserved during prograde metamorphism to at least 520 °C and

411   1 GPa, which is unlikely (Touret, 2001). Moreover, the BMC fluid inclusions are rich in N

412   species (NH_3, N_2), which seems to be an uncommon feature in fluid inclusions from oceanic

413   peridotites (Grozeva et al., 2020; Klein et al., 2019). Instead, N-rich, NH_3-bearing fluid

414   inclusions have been recently documented in CH_4-rich fluid inclusions in HP serpentinized

415   peridotites from the Alpine belt and proposed to represent a distinctive feature of subduction

416   zone serpentinizing fluids relative to mantle or (sub)seafloor fluids, especially in the presence

417   of metasediment-derived fluids (Vitale Brovarone et al., 2020). Considering the

418   microstructural and petrologic features discussed in Section 5.1, and the abundance of N

419   species, a metamorphic origin in the Taconic subduction is proposed for the studied fluid

420   inclusions.

421   The formation of lizardite and brucite as step-daughter minerals inside the fluid inclusions can

422   be interpreted (1) as a prograde, pre-antigorite inclusion-host interactions, (2) as a retrograde

423   reequilibration of antigorite during cooling of the BMC below ~400 °C with excess brucite

424   (Reaction 1), or (3) as a retrograde host-inclusion interaction below ~400 °C (Fig. 12).

425 Excluding lizardite (meta)stability due to local equilibrium/kinetic features or faster

426 antigorite-lizardite conversion in the inclusions relative to the host rock, we interpret the

427 formation of step-daughter lizardite and brucite as a retrograde host-inclusion interaction.

428 Similar interpretations have been proposed for analogous inclusions from Alpine belt (Vitale

429 Brovarone et al., 2020).

430

431 **4.2.2. Origin of the reducing potential and fluid sources**

432 Another important question is the origin the identified reduced fluids species. In particular,

433 several studies over the last decades have investigated the biotic or abiotic origin of geological

434 CH_4 and associated reduced fluid species (Etiope et al., 2011; Etiope and Sherwood Lollar,

435 2013; McCollom, 2016; Ménez et al., 2018). Ultramafic systems are generally favourable

436 environments for the genesis of abiotic CH_4 (Section 5.2.1), but other interpretations are also

437 possible.

438 For example, the abundance of metasedimentary rocks in the study area may have promoted

439 the formation of thermogenic gases during their prograde evolution. This hypothesis would

440 be also consistent with the production of NH_3 through degassing of organic matter in

441 metasedimentary rocks (Bebout and Fogel, 1992; Li et al., 2009). Biotic processes, including

442 thermogenic gas formation, typically show very light $\delta^{13}C_{CH4}$ signatures (Etiope and Sherwood

443 Lollar, 2013), whereas abiotic processes generally result in much heavier $\delta^{13}C_{CH4}$ ($\sim$-50 to 0‰)

444 (Etiope and Sherwood Lollar, 2013). In order to test this hypothesis, we performed

445 reconnaissance $\delta^{13}C$ analysis of CH_4 in the fluid inclusions (Boutier et al., in preparation). The

446 analyses yielded $\delta^{13}C$ in the range of -14‰ (±2‰) for inclusions in olivine, and -13‰ (±1‰)

447 for carbonate-hosted methane-rich inclusions from the rodingite. Even though these results

448   must be considered as preliminary test data, they seem to exclude the possibility of a pure

449   thermogenic source.

450   Following the hypothesis of an abiotic origin, two possible mechanisms for the formation of

451   CH_4 can be considered with either external or internal sources, respectively. External sources

452   correspond to the infiltration of CH_4 and other reduced species formed abiotically in other

453   geological reservoirs. A deep mantle origin for the reduced fluids detected in the BMC fluid

454   inclusions appears unlikely if the syn-inclusion, water-rich nature of the serpentinizing fluid is

455   considered. The metasedimentary formations adjacent to the BMC contain carbonate,

456   graphitic carbon, sulphides, and phyllosilicates as potential sources of the C-N-S-H fluid

457   identified in the fluid inclusions. Previous studies along the Appalachian belt have reported

458   evidence of carbon mobilization from these metasedimentary formations or their along-strike

459   equivalents. For example, Zhang *et al.*, 2018 documented metamorphic loss of isotopically

460   light carbon from the Wepawaug schists, Connecticut. The possibility for these carbonate-

461   bearing formations to generate strongly reduced fluids abiotically is not obvious —for

462   reference, water-maximum conditions in graphite-saturated fluids contain roughly equal

463   proportions of CH_4 and CO_2 (Connolly, 1995; Holloway, 1984) —. Nevertheless, evidence for

464   the circulation of CH_4-rich fluids in equivalent formations in East Central Vermont and New

465   Hampshire has been reported (Evans et al., 2002; Rumble III and Hoering, 1986).

466   Nevertheless, most petrological studies focusing on New England metasediment-derived

467   fluids point to more oxidized, CO_2-dominated aqueous fluids(Ferry, 2007; Penniston-Dorland

468   and Ferry, 2006). Alternative external sources of reduced fluids would require unidentified

469   processes, including mixing of different carbon reservoirs, or water-rock interactions

470   equivalent to those that took place in the BMC.

471   A reducing potential internal to the BMC, and in particular the hydroxylation of fresh mantle

472   peridotites during the Taconic subduction, appears the most likely interpretation for the

473   genesis of the identified reduced fluid species. The presence of Fe-Ni alloys in the BMC

474   partially serpentinized peridotites indicates that the rock recorded reducing conditions, as

475   already observed in several oceanic and ophiolitic, and some subduction zone serpentinites

476   (Evans et al., 2017; Frost, 1985; Klein and Bach, 2009; Vitale Brovarone et al., 2020). High-

477   pressure syn-serpentinization reducing conditions are also suggested by the thermodynamic

478   modelling results presented in this study, which indicates fO$_2$ values as low as -3.2 ΔQFM at

479   400 °C and 1 GPa to -1.2 ΔQFM at 450 °C and 1 GPa, and the formation of significant amounts

480   of H$_2$ in the fluid (Fig. 10C). The interaction of this H$_2$ with dissolved carbon, nitrogen, and

481   sulphur species present in the serpentinizing fluid, could have favoured the formation of CH$_4$

482   H$_2$S, and NH$_3$ from more oxidized species. For NH$_3$, the modelling also indicates that this

483   species is already the dominant N species in the infiltrating fluid buffered at QFM. This feature

484   suggests that the N$_2$ detected in the fluid is most likely formed through post-entrapment

485   respeciation of NH$_3$, unless the serpentinizing fluid was more oxidized than QFM. The absence

486   of detectable H$_2$O in the fluid inclusions is interpreted to result from host-inclusion interaction

487   and formation of step-daughter lizardite and brucite, or by the preferential entrapment of

488   immiscible reduced gases relative to aqueous fluids (Huang et al., 2017; Vitale Brovarone et

489   al., 2017). The absence of residual H$_2$ in the fluid inclusions may be explained by the much

490   faster diffusion H$_2$ relative to other fluid species through the host olivine, or by selective

491   leakage.

492   The most plausible sources of serpentinizing fluid were the metasedimentary formations

493   surrounding the BMC complex. These rock types host substantial amounts of subducted

494   carbon, sulphur, and nitrogen (Bebout and Fogel, 1992; Evans et al., 2014; Kelemen and

495 Manning, 2015; Plank and Manning, 2019). An ultramafic source internal to the BMC would

496 not be consistent with the general retention of N during prograde metamorphism and

497 dehydration of serpentinites (Halama et al., 2014). The hypothesis of a metasediment-derived

498 serpentinizing fluid was also suggested by previous oxygen and hydrogen isotopic data on

499 antigorite from the BMC complex (Wenner and Taylor, 1974, 1971). Moreover, the authors

500 proposed antigorite-magnetite equilibration T in the range of 220-460 °C, which is consistent

501 with the prograde P-T of the BMC (Fig. 12). This supports the interpretation of a subduction-

502 related serpentinization related to the infiltration of metasedimentary-derived fluids in a

503 rather dry ultramafic body.

504 **5. Conclusions**

505 Mineralogical, microstructural, and fluid inclusion study of variably serpentinized dunite from

506 the Belvidere Mountain Complex, Appalachian belt, Northern Vermont, provides insight into

507 the process of high-pressure serpentinization in subduction zone and the related fluid-rock

508 redox patterns. Although the BMC underwent a complex tectonic evolution potentially

509 characterized by multiple stages of hydration from the (sub)seafloor to subduction and

510 exhumation, the collected data point to a major event of high-pressure serpentinization that

511 took place in the Appalachian subduction zone. Metamorphic olivine in the BMC

512 serpentinized peridotite is interpreted as the product of rock hydration rather than

513 dehydration, linked to the high-pressure serpentinization event. Our data support the

514 hypothesis that the methane observed in olivine-hosted secondary fluid inclusions is

515 genetically linked to serpentinization in the antigorite stability field consistent with the high-

516 pressure portion of the prograde or retrograde P-T path of the BMC. This favors an abiotic

517 origin for this methane, even though a biotic origin for the C source cannot be excluded. The

518   C- and N-rich composition of fluid inclusions suggests a metasediment-derived origin for the

519   serpentinizing fluid. The high-pressure serpentinization and related abiotic methanogenesis

520   place the Belvidere mountain complex as a suitable proxy for the study of mantle wedge

521   serpentinization. This study confirms the importance of fluid mobility in deep seated

522   ultramafic body in subduction zones for the mobility of C, H, and N, and their implications on

523   large-scale geochemical cycling.

524   **6. Acknowledgments**

529   **7. References**

530   Andréani, M., Mével, C., Boullier, A.-M., Escartin, J., 2007. Dynamic control on serpentine
531   crystallization in veins: Constraints on hydration processes in oceanic peridotites. Geochem.
532   Geophys. Geosystems 8.
533   Andreani, M., Munoz, M., Marcaillou, C., Delacour, A., 2013. µXANES study of iron redox state in
534   serpentine during oceanic serpentinization. Lithos 178, 70–83.
535   Arai, S., Ishimaru, S., Mizukami, T., 2012. Methane and propane micro-inclusions in olivine in
536   titanoclinohumite-bearing dunites from the Sanbagawa high-P metamorphic belt, Japan:
537   Hydrocarbon activity in a subduction zone and Ti mobility. Earth Planet. Sci. Lett. 353, 1–11.
538   Auzende, A.-L., Daniel, I., Reynard, B., Lemaire, C., Guyot, F., 2004. High-pressure behaviour of
539   serpentine minerals: a Raman spectroscopic study. Phys. Chem. Miner. 31, 269–277.
540   Bebout, G.E., Fogel, M.L., 1992. Nitrogen-isotope compositions of metasedimentary rocks in the
541   Catalina Schist, California: implications for metamorphic devolatilization history. Geochim.
542   Cosmochim. Acta 56, 2839–2849.
543   Bebout, G.E., Penniston-Dorland, S.C., 2016. Fluid and mass transfer at subduction interfaces—The
544   field metamorphic record. Lithos 240–243, 228–258.
545   https://doi.org/10.1016/j.lithos.2015.10.007
546   Berkesi, M., Hidas, K., Guzmics, T., Dubessy, J., Bodnar, R.J., Szabó, C., Vajna, B., Tsunogae, T., 2009.
547   Detection of small amounts of H2O in CO2-rich fluid inclusions using Raman spectroscopy. J.
548   Raman Spectrosc. Int. J. Orig. Work Asp. Raman Spectrosc. High. Order Process. Also
549   Brillouin Rayleigh Scatt. 40, 1461–1463.
550   Berman, R.G., 1988. Internally-consistent thermodynamic data for minerals in the system Na2O-
551   K2O-CaO-MgO-FeO-Fe2O3-Al2O3-SiO2-TiO2-H2O-CO2. J. Petrol. 29, 445–522.

552   Berndt, M.E., Allen, D.E., Seyfried Jr, W.E., 1996. Reduction of CO2 during serpentinization of olivine
553   at 300 C and 500 bar. Geology 24, 351–354.
554   Cannat, M., Fontaine, F., Escartin, J., 2010. Serpentinization and associated hydrogen and methane
555   fluxes at slow spreading ridges. Divers. Hydrothermal Syst. Slow Spreading Ocean Ridges
556   188, 241–264.
557   Castonguay, S., Kim, J., Thompson, P.J., Gale, M.H., Joyce, N., Laird, J., Doolan, B.L., 2012. Timing of
558   tectonometamorphism across the Green Mountain anticlinorium, northern Vermont
559   Appalachians: 40Ar/39Ar data and correlations with southern Quebec. GSA Bull. 124, 352–
560   367. https://doi.org/10.1130/B30487.1
561   Caumon, M.-C., Tarantola, A., Wang, W., 2019. Raman spectra of gas mixtures in fluid inclusions:
562   Effect of quartz birefringence on composition measurement. J. Raman Spectrosc.
563   Cesare, B., 1995. Graphite precipitation in C—O—H fluid inclusions: closed system compositional and
564   density changes, and thermobarometric implications. Contrib. Mineral. Petrol. 122, 25–33.
565   Chew, D.M., van Staal, C.R., 2014. The ocean–continent transition zones along the Appalachian–
566   Caledonian Margin of Laurentia: Examples of large-scale hyperextension during the opening
567   of the Iapetus Ocean. Geosci. Can. 41, 165–185.
568   Chidester, A.H., Albee, A.L., Cady, W.M., 1978. Petrology, structure, and genesis of the asbestos-
569   bearing ultramafic rocks of the Belvidere Mountain area in Vermont. US Govt. Print. Off.,.
570   Connolly, J.A.D., 1995. Phase diagram methods for graphitic rocks and application to the system C-
571   O- H- FeO- TiO 2- SiO 2. Contrib. Mineral. Petrol. 119, 94–116.
572   Dandar, O., Okamoto, A., Uno, M., Oyanagi, R., Nagaya, T., Burenjargal, U., Miyamoto, T., Tsuchiya,
573   N., 2019. Formation of secondary olivine after orthopyroxene during hydration of mantle
574   wedge: evidence from the Khantaishir Ophiolite, western Mongolia. Contrib. Mineral. Petrol.
575   174, 86.
576   Debret, B., Nicollet, C., Andreani, M., Schwartz, S., Godard, M., 2013. Three steps of serpentinization
577   in an eclogitized oceanic serpentinization front (Lanzo Massif–Western Alps). J. Metamorph.
578   Geol. 31, 165–186.
579   Deschamps, F., Godard, M., Guillot, S., Hattori, K., 2013. Geochemistry of subduction zone
580   serpentinites: A review. Lithos 178, 96–127.
581   Doolan, B.L., Gale, M.H., Gale, P.N., Hoar, R.S., St-Julien, P., 1982. Geology of the Quebec re-entrant:
582   possible constraints from early rifts and the Vermont-Quebec serpentine belt. Major Struct.
583   Zones Faults North. Appalach. Ed. P St-Julien J Béland Geol. Assoc. Can. Spec. Pap. 24, 87–
584   115.
585   Etiope, G., Schoell, M., Hosgörmez, H., 2011. Abiotic methane flux from the Chimaera seep and
586   Tekirova ophiolites (Turkey): understanding gas exhalation from low temperature
587   serpentinization and implications for Mars. Earth Planet. Sci. Lett. 310, 96–104.
588   Etiope, G., Sherwood Lollar, B., 2013. Abiotic methane on Earth. Rev. Geophys. 51, 276–299.
589   Evans, B.W., 2010. Lizardite versus antigorite serpentinite: Magnetite, hydrogen, and life (?).
590   Geology 38, 879–882.
591   Evans, B.W., 2008. Control of the products of serpentinization by the Fe2+ Mg- 1 exchange potential
592   of olivine and orthopyroxene. J. Petrol. 49, 1873–1887.
593   Evans, B.W., 2004. The serpentinite multisystem revisited: chrysotile is metastable. Int. Geol. Rev.
594   46, 479–506.
595   Evans, K.A., Bickle, M.J., Skelton, A.D.L., Hall, M., Chapman, H., 2002. Reductive deposition of
596   graphite at lithological margins in East Central Vermont: a Sr, C and O isotope study. J.
597   Metamorph. Geol. 20, 781–798.
598   Evans, K.A., Reddy, S.M., Tomkins, A.G., Crossley, R.J., Frost, B.R., 2017. Effects of geodynamic
599   setting on the redox state of fluids released by subducted mantle lithosphere. Lithos 278–
600   281, 26–42. https://doi.org/10.1016/j.lithos.2016.12.023
601   Evans, K.A., Tomkins, A.G., Cliff, J., Fiorentini, M.L., 2014. Insights into subduction zone sulfur
602   recycling from isotopic analysis of eclogite-hosted sulfides. Chem. Geol. 365, 1–19.

603 Ferry, J.M., 2007. The role of volatile transport by diffusion and dispersion in driving biotite-forming
604   reactions during regional metamorphism of the Gile Mountain Formation, Vermont. Am.
605   Mineral. 92, 1288–1302.
606 Frezzotti, M.L., Tecce, F., Casagli, A., 2012. Raman spectroscopy for fluid inclusion analysis. J.
607   Geochem. Explor. 112, 1–20.
608 Frost, B.R., 1985. On the stability of sulfides, oxides, and native metals in serpentinite. J. Petrol. 26,
609   31–63.
610 Frost, B.R., Beard, J.S., 2007. On silica activity and serpentinization. J. Petrol. 48, 1351–1368.
611 Früh-Green, G.L., Connolly, J.A., Plas, A., Kelley, D.S., Grobéty, B., 2004. Serpentinization of oceanic
612   peridotites: implications for geochemical cycles and biological activity. Subseafloor
613   Biosphere -Ocean Ridges 144, 119–136.
614 Gale, M.H., 2007. Bedrock Geologic Map of the Hazens Notch and Portions of the Eden and Lowell
615   Quadrangles, Vermont. Vt. Geol. Surv., Vermont geological open file report VG07-2, plate 1.
616 Gale, M.H., 1986. Geologic map of the Belvidere Mountain area, Eden and Lowell, Vermont (USGS
617   Numbered Series No. 1560), IMAP.
618 Gale, M.H., 1980. Geology of the Belvidere Mountain Complex, Eden and Lowell, Vermont. US
619   Geological Survey,.
620 Grozeva, N.G., Klein, F., Seewald, J.S., Sylva, S.P., 2020. Chemical and isotopic analyses of
621   hydrocarbon-bearing fluid inclusions in olivine-rich rocks. Philos. Trans. R. Soc. A 378,
622   20180431.
623 Guillot, S., Hattori, K.H., de Sigoyer, J., 2000. Mantle wedge serpentinization and exhumation of
624   eclogites: insights from eastern Ladakh, northwest Himalaya. Geology 28, 199–202.
625 Guillot, S., Schwartz, S., Reynard, B., Agard, P., Prigent, C., 2015. Tectonic significance of
626   serpentinites. Tectonophysics 646, 1–19.
627 Halama, R., Bebout, G.E., John, T., Scambelluri, M., 2014. Nitrogen recycling in subducted mantle
628   rocks and implications for the global nitrogen cycle. Int. J. Earth Sci. 103, 2081–2099.
629 Hibbard, J.P., Van Staal, C.R., Rankin, D.W., Williams, H., 2006. Lithotectonic map of the Appalachian
630   orogen, Canada–United States of America. Geol. Surv. Can. Map A 2096, 2.
631 Holloway, J.R., 1984. Graphite-CH4-H2O-CO2 equilibria at low-grade metamorphic conditions.
632   Geology 12, 455–458.
633 Holm, N.G., Charlou, J.L., 2001. Initial indications of abiotic formation of hydrocarbons in the
634   Rainbow ultramafic hydrothermal system, Mid-Atlantic Ridge. Earth Planet. Sci. Lett. 191, 1–
635   8.
636 Honsberger, I.W., 2015. Metamorphism, deformation, geochemistry, and tectonics of exhumed
637   ultramafic and mafic rocks in the central and north-central Vermont Appalachians.
638 Honsberger, I.W., Laird, J., Thompson, P.J., 2017. A tectonized ultramafic-mafic-pelitic package in
639   Stockbridge, Vermont: Metamorphism resulting from subduction and exhumation. Am. J.
640   Sci. 317, 1019–1047.
641 Huang, F., Daniel, I., Cardon, H., Montagnac, G., Sverjensky, D.A., 2017. Immiscible hydrocarbon
642   fluids in the deep carbon cycle. Nat. Commun. 8, 1–8.
643 Iyer, K., Austrheim, H., John, T., Jamtveit, B., 2008. Serpentinization of the oceanic lithosphere and
644   some geochemical consequences: constraints from the Leka Ophiolite Complex, Norway.
645   Chem. Geol. 249, 66–90.
646 Karabinos, P., Samson, S.D., Hepburn, J.C., Stoll, H.M., 1998. Taconian orogeny in the New England
647   Appalachians: Collision between Laurentia and the Shelburne Falls arc. Geology 26, 215–218.
648   https://doi.org/10.1130/0091-7613(1998)026<0215:TOITNE>2.3.CO;2
649 Kelemen, P.B., Manning, C.E., 2015. Reevaluating carbon fluxes in subduction zones, what goes
650   down, mostly comes up. Proc. Natl. Acad. Sci. 112, E3997–E4006.
651   https://doi.org/10.1073/pnas.1507889112
652 Kelley, D.S., Karson, J.A., Früh-Green, G.L., Yoerger, D.R., Shank, T.M., Butterfield, D.A., Hayes, J.M.,
653   Schrenk, M.O., Olson, E.J., Proskurowski, G., Jakuba, M., Bradley, A., Larson, B., Ludwig, K.,

654   Glickson, D., Buckman, K., Bradley, A.S., Brazelton, W.J., Roe, K., Elend, M.J., Delacour, A.,
655   Bernasconi, S.M., Lilley, M.D., Baross, J.A., Summons, R.E., Sylva, S.P., 2005. A Serpentinite-
656   Hosted Ecosystem: The Lost City Hydrothermal Field. Science 307, 1428–1434.
657   https://doi.org/10.1126/science.1102556

658   Kempf, E.D., Hermann, J., 2018. Hydrogen incorporation and retention in metamorphic olivine
659   during subduction: Implications for the deep water cycle. Geology 46, 571–574.

660   Klein, F., Bach, W., 2009. Fe–Ni–Co–O–S phase relations in peridotite–seawater interactions. J.
661   Petrol. 50, 37–59.

662   Klein, F., Bach, W., Humphris, S.E., Kahl, W.-A., Jöns, N., Moskowitz, B., Berquó, T.S., 2014. Magnetite
663   in seafloor serpentinite—Some like it hot. Geology 42, 135–138.

664   Klein, F., Bach, W., McCollom, T.M., 2013. Compositional controls on hydrogen generation during
665   serpentinization of ultramafic rocks. Lithos 178, 55–69.

666   Klein, F., Grozeva, N.G., Seewald, J.S., 2019. Abiotic methane synthesis and serpentinization in
667   olivine-hosted fluid inclusions. Proc. Natl. Acad. Sci. 116, 17666–17672.

668   Laird, J., Lanphere, M.A., Albee, A.L., 1984. Distribution of Ordovician and Devonian metamorphism
669   in mafic and pelitic schists from northern Vermont. Am. J. Sci. 284, 376–413.

670   Laird, J., Trzcienski, W.E., Bothner, W.A., Cheney, J.T., Hepburn, J.C., 1993. High-pressure, Taconian,
671   and subsequent polymetamorphism of southern Quebec and northern Vermont. Contrib.
672   Dep. Univ. Mass. 67, 1–32.

673   Lamadrid, H.M., Rimstidt, J.D., Schwarzenbach, E.M., Klein, F., Ulrich, S., Dolocan, A., Bodnar, R.J.,
674   2017. Effect of water activity on rates of serpentinization of olivine. Nat. Commun. 8, 1–9.

675   Li, L., Cartigny, P., Ader, M., 2009. Kinetic nitrogen isotope fractionation associated with thermal
676   decomposition of NH3: Experimental results and potential applications to trace the origin of
677   N2 in natural gas and hydrothermal systems. Geochim. Cosmochim. Acta 73, 6282–6297.

678   Majumdar, A.S., Hövelmann, J., Vollmer, C., Berndt, J., Mondal, S.K., Putnis, A., 2016. Formation of
679   Mg-rich olivine pseudomorphs in serpentinized dunite from the Mesoarchean Nuasahi
680   Massif, Eastern India: Insights into the evolution of fluid composition at the mineral–fluid
681   interface. J. Petrol. 57, 3–26.

682   McCollom, T.M., 2016. Abiotic methane formation during experimental serpentinization of olivine.
683   Proc. Natl. Acad. Sci. 113, 13965–13970.

684   Ménez, B., Pisapia, C., Andreani, M., Jamme, F., Vanbellingen, Q.P., Brunelle, A., Richard, L., Dumas,
685   P., Réfrégiers, M., 2018. Abiotic synthesis of amino acids in the recesses of the oceanic
686   lithosphere. Nature 564, 59–63. https://doi.org/10.1038/s41586-018-0684-z

687   Mével, C., 2003. Serpentinization of abyssal peridotites at mid-ocean ridges. Comptes Rendus
688   Geosci. 335, 825–852.

689   Moody, J.B., 1976. Serpentinization: a review. Lithos 9, 125–138.

690   Nozaka, T., 2018. Compositional variation of olivine related to high–temperature serpentinization of
691   peridotites: Evidence from the Oeyama ophiolite. J. Mineral. Petrol. Sci. 180420.

692   Nozaka, T., 2003. Compositional heterogeneity of olivine in thermally metamorphosed serpentinite
693   from Southwest Japan. Am. Mineral. 88, 1377–1384.

694   Penniston-Dorland, S.C., Ferry, J.M., 2006. Development of spatial variations in reaction progress
695   during regional metamorphism of micaceous carbonate rocks, northern New England. Am. J.
696   Sci. 306, 475–524.

697   Plank, T., Manning, C.E., 2019. Subducting carbon. Nature 574, 343–352.

698   Plümper, O., John, T., Podladchikov, Y.Y., Vrijmoed, J.C., Scambelluri, M., 2017. Fluid escape from
699   subduction zones controlled by channel-forming reactive porosity. Nat. Geosci. 10, 150–156.
700   https://doi.org/10.1038/ngeo2865

701   Plümper, O., King, H.E., Vollmer, C., Ramasse, Q., Jung, H., Austrheim, H., 2012a. The legacy of
702   crystal-plastic deformation in olivine: high-diffusivity pathways during serpentinization.
703   Contrib. Mineral. Petrol. 163, 701–724.

704 Plümper, O., Piazolo, S., Austrheim, H., 2012b. Olivine pseudomorphs after serpentinized
705   orthopyroxene record transient oceanic lithospheric mantle dehydration (Leka Ophiolite
706   Complex, Norway). J. Petrol. 53, 1943–1968.
707 Rouméjon, S., Andreani, M., Früh-Green, G.L., 2019. Antigorite crystallization during oceanic
708   retrograde serpentinization of abyssal peridotites. Contrib. Mineral. Petrol. 174, 60.
709 Rumble III, D., Hoering, T.C., 1986. Carbon isotope geochemistry of graphite vein deposits from New
710   Hampshire, USA. Geochim. Cosmochim. Acta 50, 1239–1247.
711 Scambelluri, M., Müntener, O., Hermann, J., Piccardo, G.B., Trommsdorff, V., 1995. Subduction of
712   water into the mantle: history of an Alpine peridotite. Geology 23, 459–462.
713 Scambelluri, M., Strating, E.H., Piccardo, G.B., Vissers, R.L.M., Rampone, E., 1991. Alpine olivine-and
714   titanian clinohumite-bearing assemblages in the Erro-Tobbio peridotite (Voltri Massif, NW
715   Italy). J. Metamorph. Geol. 9, 79–91.
716 Scambelluri, M., Tonarini, S., 2012. Boron isotope evidence for shallow fluid transfer across
717   subduction zones by serpentinized mantle. Geology 40, 907–910.
718 Schrenk, M.O., Brazelton, W.J., Lang, S.Q., 2013. Serpentinization, carbon, and deep life. Rev.
719   Mineral. Geochem. 75, 575–606.
720 Schwartz, S., Guillot, S., Reynard, B., Lafay, R., Debret, B., Nicollet, C., Lanari, P., Auzende, A.L., 2013.
721   Pressure–temperature estimates of the lizardite/antigorite transition in high pressure
722   serpentinites. Lithos 178, 197–210.
723 Seyfried Jr, W.E., Foustoukos, D.I., Fu, Q., 2007. Redox evolution and mass transfer during
724   serpentinization: An experimental and theoretical study at 200 C, 500 bar with implications
725   for ultramafic-hosted hydrothermal systems at Mid-Ocean Ridges. Geochim. Cosmochim.
726   Acta 71, 3872–3886.
727 Shen, T., Hermann, J., Zhang, L., Lü, Z., Padrón-Navarta, J.A., Xia, B., Bader, T., 2015. UHP
728   metamorphism documented in Ti-chondrodite-and Ti-clinohumite-bearing serpentinized
729   ultramafic rocks from Chinese southwestern Tianshan. J. Petrol. 56, 1425–1458.
730 Sleep, N.H., Bird, D.K., 2007. Niches of the pre-photosynthetic biosphere and geologic preservation
731   of Earth's earliest ecology. Geobiology 5, 101–117.
732 Stanley, R.S., Roy, D.L., Hatch, N.L., Knapp, D.A., 1984. Evidence for tectonic emplacement of
733   ultramafic and associated rocks in the pre-Silurian eugeoclinal belt of western New England;
734   vestiges of an ancient accretionary wedge. Am. J. Sci. 284, 559–595.
735   https://doi.org/10.2475/ajs.284.4-5.559
736 Sverjensky, D.A., Harrison, B., Azzolini, D., 2014. Water in the deep Earth: the dielectric constant and
737   the solubilities of quartz and corundum to 60 kb and 1200 C. Geochim. Cosmochim. Acta
738   129, 125–145.
739 Touret, J.L.R., 2001. Fluids in metamorphic rocks. Lithos 55, 1–25.
740 Trommsdorff, V., Evans, B.W., 1974. Alpine metamorphism of peridotitic rocks. Schweiz Min Pet Mitt
741   54, 333–352.
742 Van Baalen, M.R., Mossman, B.T., Gunter, M.E., Francis, C.A., 2009. Environmental Geology of
743   Belvidere Mt.
744 Vitale Brovarone, A., Martinez, I., Elmaleh, A., Compagnoni, R., Chaduteau, C., Ferraris, C., Esteve, I.,
745   2017. Massive production of abiotic methane during subduction evidenced in
746   metamorphosed ophicarbonates from the Italian Alps. Nat. Commun. 8, 14134.
747 Vitale Brovarone, A., Sverjensky, D.A., Piccoli, F., Ressico, F., Giovannelli, D., Daniel, I., 2020.
748   Subduction hides high-pressure sources of energy that may feed the deep subsurface
749   biosphere. Nat. Commun. 11, 1–11.
750 Viti, C., Mellini, M., Rumori, C., 2005. Exsolution and hydration of pyroxenes from partially
751   serpentinized harzburgites. Mineral. Mag. 69, 491–507.
752 Wada, I., Wang, K., He, J., Hyndman, R.D., 2008. Weakening of the subduction interface and its
753   effects on surface heat flow, slab dehydration, and mantle wedge serpentinization. J.
754   Geophys. Res. Solid Earth 113.

755 Wenner, D.B., Taylor, H.P., 1974. D/H and O18/O16 studies of serpentinization of ultramaflc rocks.
756   Geochim. Cosmochim. Acta 38, 1255–1286.
757 Wenner, D.B., Taylor, H.P., 1971. Temperatures of serpentinization of ultramafic rocks based on O
758   18/O 16 fractionation between coexisting serpentine and magnetite. Contrib. Mineral.
759   Petrol. 32, 165–185.
760 Wolery, Tj., Jarek, R.L., 2003. Software user's manual: EQ3/6, version 8.0. Softw. Doc. 8–0.
761 Zhang, S., Ague, J.J., Vitale Brovarone, A., 2018. Degassing of organic carbon during regional
762   metamorphism of pelites, Wepawaug Schist, Connecticut, USA. Chem. Geol. 490, 30–44.
763   https://doi.org/10.1016/j.chemgeo.2018.05.003
764

1 *Fig. 1: A: Simplified geological map of Vermont, modified from Hibbard et al., (2006). B:*

2 *Simplified bedrock geologic map of the Belvidere Mountain Complex and the surrounding*

3 *formations. Modified after Hibbard et al., (2006). Units description from Hibbard et al., (2006)*

4 *and Gale, (2007).*

5 *Fig. 2: A-B: Photographs of the Belvidere serpentinized peridotite in outcrop. C: Weakly*

6 *serpentinized dunite (samples V18-2a and V18-2b). D: Serpentinized dunite, with boudinaged*

7 *meta-gabbro (samples V18-3a and V18-3b).*

8 *Fig. 3: A: Photomicrograph of a partially serpentinized dunite. B: Partial replacement of*

9 *primary chromian spinel by magnetite and chlorite. C: Partial replacement of olivine by*

10 *antigorite. D: Inferred primary orthopyroxene being pseudomorphically replaced by*

11 *metamorphic olivine. See also Figure 5B. E: Photomicrograph of a pyroxenite layer included in*

12 *the Belvidere peridotite. The photomicrograph shows radial diopside aggregate*

13 *pseudomorphic on primary clinopyroxene. Partially serpentinized olivine is also visible. F:*

14 *Magnetite-rich diopside pseudomorphosis on primary clinopyroxene. Note the growth of*

15 *metamorphic olivine at the rim of the clinopyroxene site. See Figure 5A for SEM-based*

16 *backscattered electron image. G: Metamorphic diopside replacing primary clinopyroxene. In*

17 *this case, note the growth of metamorphic olivine along fractures cutting the*

18 *pseudomorphosis. See Figure 5F for SEM-based backscattered electron image. H: Relict of*

19 *metamorphic olivine pseudomorphic on primary clinopyroxene. The metamorphic olivine is*

20 *then partially replaced by serpentine + brucite + magnetite. A-D: Sample V18-2b, E-G: Sample*

21 *V18-3a; H: sample V18-B3. P-Ol: primary olivine, M-Ol: metamorphic olivine, Atg: antigorite,*

22 *Chl: chlorite, Mgt: magnetite, Di: diopside, Chr: chromite, Br: brucite, Ctl: chrysotile.*

23 **Fig. 4**: *Raman spectra of solid phases. A: Primary olivine. B Antigorite overgrowing primary*

24 *olivine. C: Antigorite core (Atg1) and rim (Atg2) (see Fig. 5A). D: Brucite.*

25 **Fig. 5**: *SEM-BSE images of samples V18-2b,V18-3a and V18-B3. A: Microstructural patterns of*

26 *serpentinization. Two generations of serpentine can be observed based on the BSE contract, a*

27 *bright core (Atg1) and a dark rim (Atg2). Note also the striped zonation of primary olivine and*

28 *the formation of metamorphic olivine. B: Replacement of an inferred primary orthopyroxene*

29 *crystal by metamorphic olivine. The close-up shows the preservation of clinopyroxene relicts*

30 *interpreted as exsolutions inside the former orthopyroxene. C: Formation of at the expense of*

31 *metamorphic. D: Composite aggregate of Fe-Ni and Fe-Cu-Ni alloys and Ni sulphide. E: Growth*

32 *of metamorphic olivine around a diopside-rich primary clinophyroxene pseudomorphosis. A*

33 *primary chromina spinel partially converted into magnetite can also be observed. F:*

34 *Metamorphic diopside replacing primary clinopyroxene. Note the presence of antigorite +*

35 *metamorphic olivine ± magnetite along the fractures. In this case, metamorphic olivine*

36 *occupies the centre of the fractures and is not in contact with diopside, whereas the*

37 *metamorphic olivine rimming the primary clinopyroxene site is in contact with it. G:*

38 *Metamorphic olivine growing at the expense of metamorphic diopside (former primary*

39 *clinopyroxene). The microstructure suggests the former presence of serpentine needles*

40 *replacing the clinopyroxene and successively replaced by metamorphic olivine. Both Atg1 and*

41 *Atg2 antigorite generations are present. H: Relict of metamorphic olivine formed at the*

42 *expense of a primary orthopyroxene site in V18-3b. The metamorphic olivine is partially*

43 *converted into brucite + serpentine. P-Ol: primary olivine M-Ol: metamorphic olivine Px:*

44 *pyroxene Di: diopside Mtg: magnetite Chr: chromite Atg: antigorite Br: brucite Ctl: chrysotile*

45 *NiFeS: nickel and iron sulphite. The presence of antigorite was confirmed by Raman*

46 *spectroscopy.*

47 ***Fig. 6***: *Mg# versus MnO (wt%) diagram showing the compositional variation of primary and*

48 *metamorphic olivine. The Mn-richest cluster of metamorphic olivine belongs to sample V18-*

49 *B3 (fully serpentinized peridotite). Background data from Arai et al., (2012); Dandar et al.,*

50 *(2019); Debret et al., (2013); Iyer et al., (2008); Nozaka, (2018); Plümper et al., (2012b);*

51 *Scambelluri et al., (1995); Shen et al., (2015).*

52 ***Fig. 7***: *Photomicrographs of methane-rich fluid inclusion trails in olivine from sample V18-2a.*

53 *Black arrows indicate fluid inclusion trails. A: Inclusion trail being cut by antigorite veinlets. B:*

54 *Inclusion trail limited by antigorite veins. C: Secondary trail of fluid inclusions propagating*

55 *from an antigorite veinlet. D: Photomicrograph showing a fluid-inclusion-rich olivine*

56 *aggregate. E: Close up of the methane-rich fluid inclusions. F: Close up of a graphite bearing*

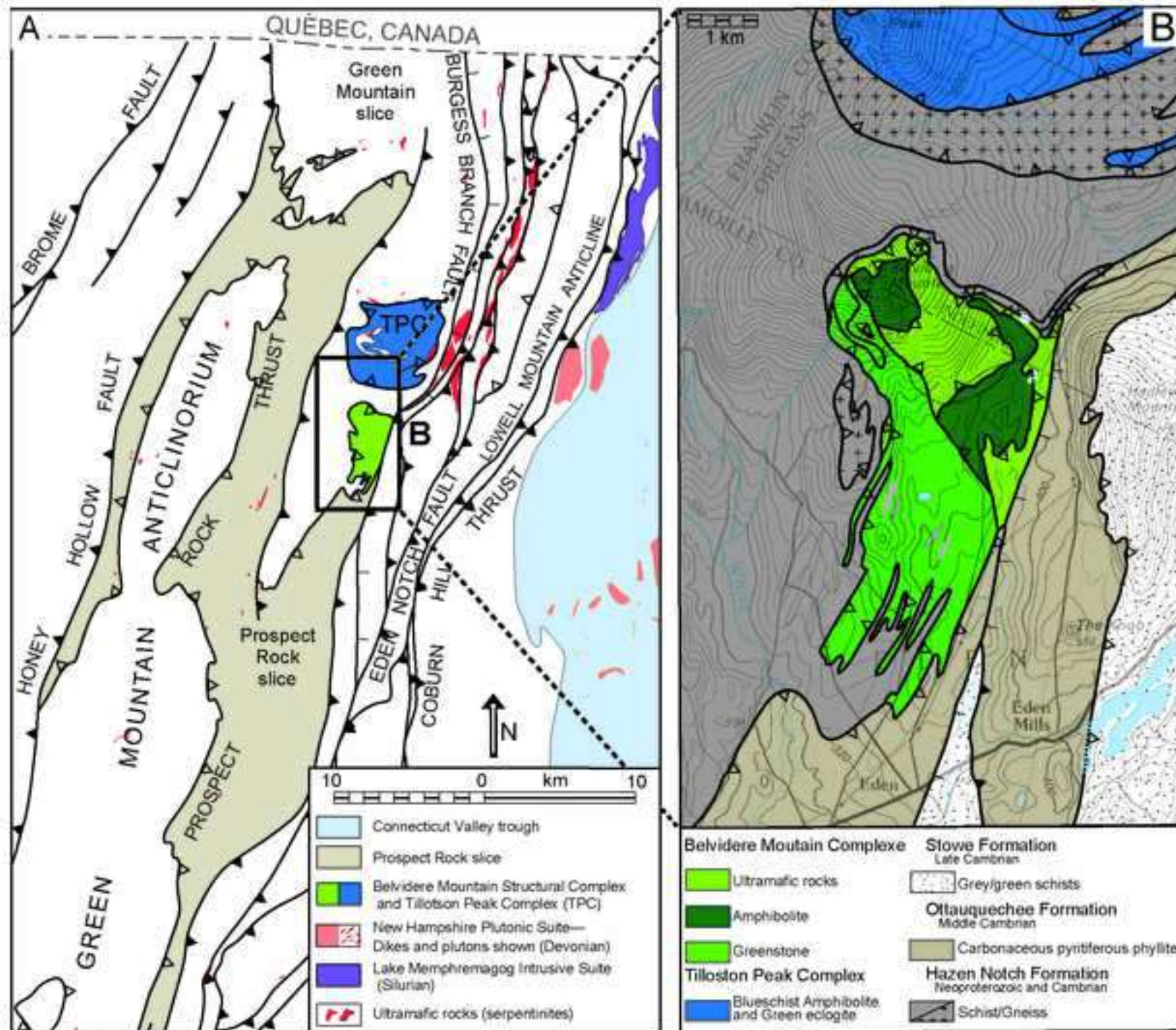57 *fluid inclusion (red arrow), as confirmed by Raman spectroscopy in (Fig. 8B).*

58 ***Fig. 8***: *Raman spectra of fluid inclusions and step-daughter solid phases. A: Inclusion showing*

59 *a marked CH_4 band and minor peaks of N_2 NH_3 and S-H bond. Lizardite and brucite O-H bands*

60 *are also observed. B: Graphite in fluid inclusions (see Fig. 6D). C: Methane-rich fluid inclusion*

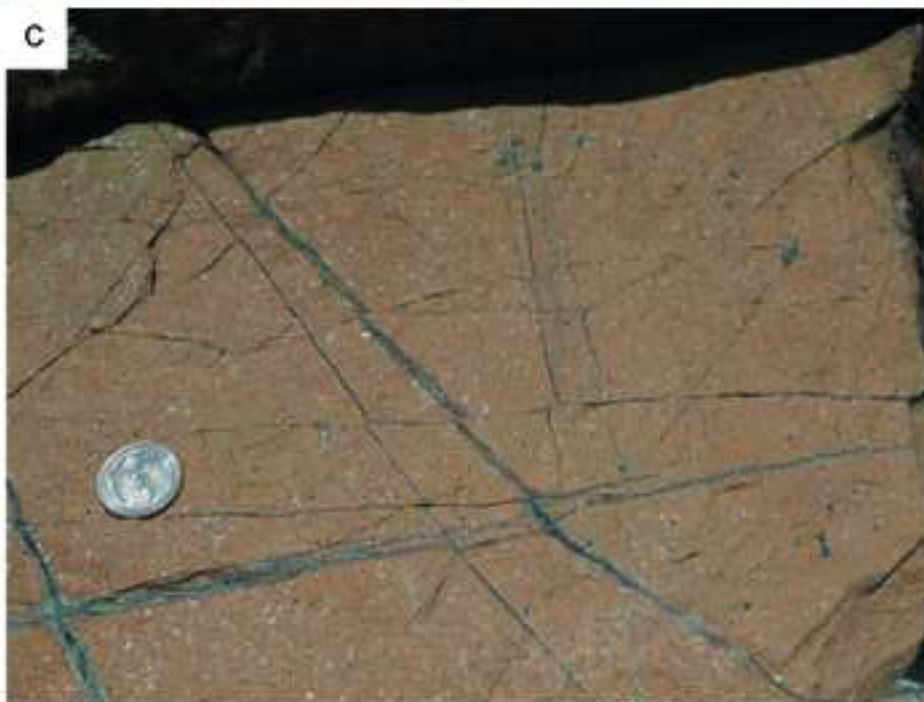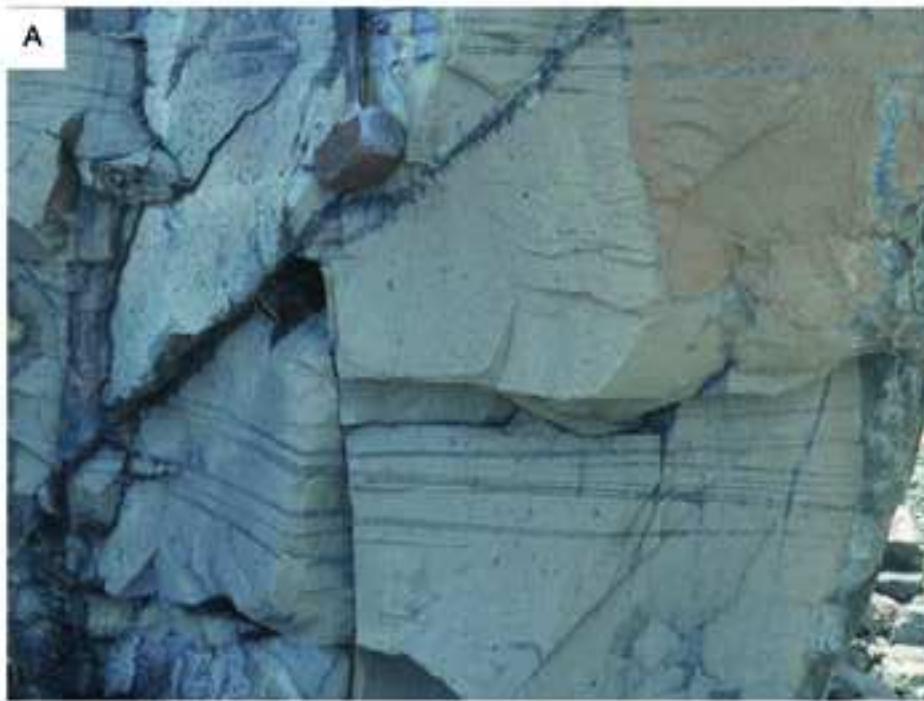61 *with a close up of O-H bonds of lizardite and brucite.*

62 ***Fig. 9***: *Calculated molar fraction of CH_4, N_2, H_2S and NH_3 from Raman scattering cross-section*

63 *and the instrumental efficiency of each species. See Frezzotti et al., (2012) for methodology.*

64 ***Fig. 10***: *Thermodynamic modelling of HP serpentinization of dunite and related mineralogical*

65 *and fluid evolution. A: Mineralogical evolution during serpentinization at 450 °C and 1 GPa.*

66 *Representative microstructures of the main reaction steps are proposed as observed in the*

67 *natural samples. B: Evolution of the nitrogen and sulphur fluid speciation as a function of the*

68 *reaction progress presented in A. C: Evolution of the fO_2 and H_2, CH_4, and CO_2 concentrations*

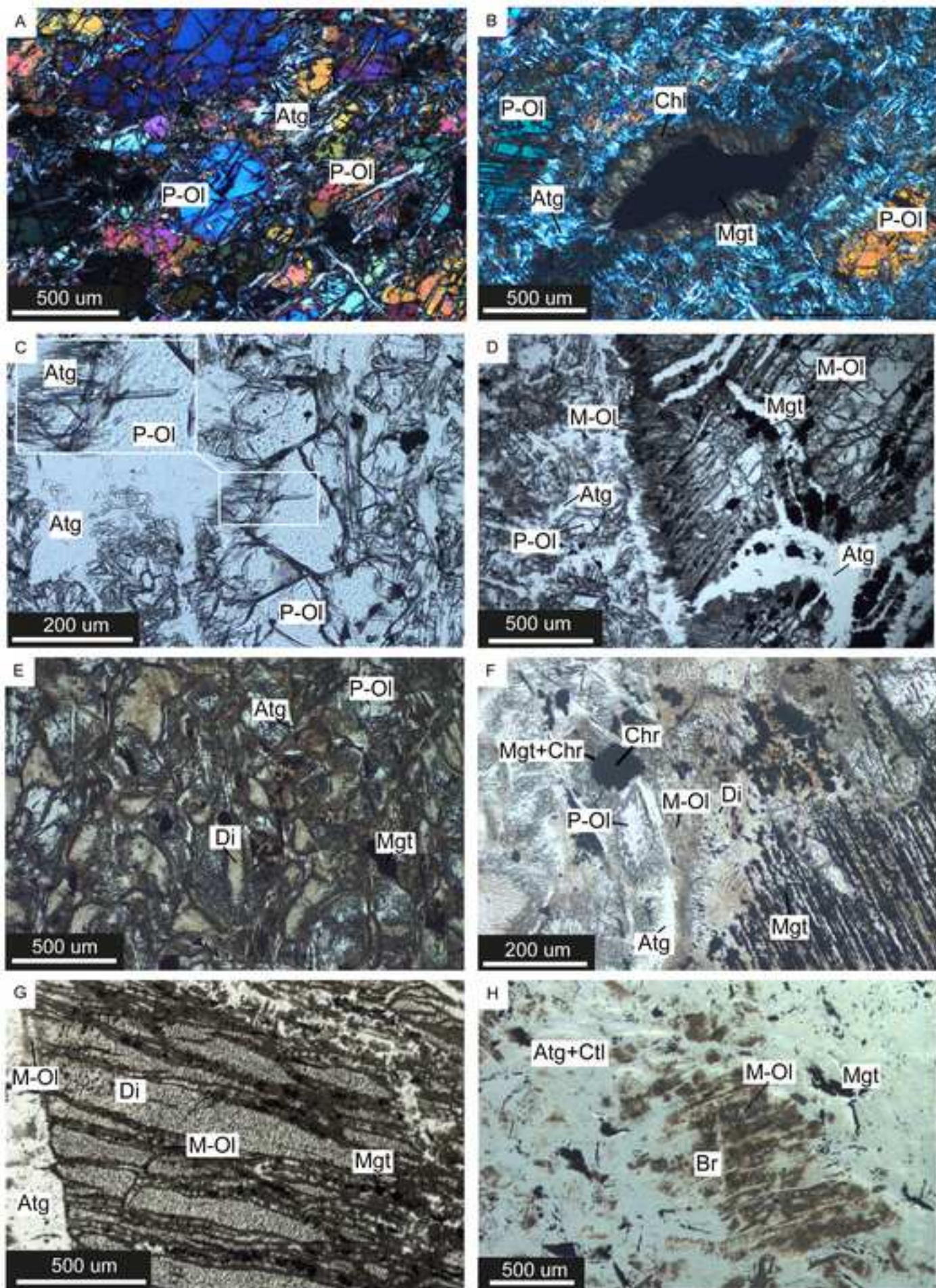69 *in the fluid as a function of the reaction progress presented in A.*

70 *Fig. 11: Reconstruction of the mineralogical evolution of the BMC partially serpentinized*

71 *peridotite. An early step of serpentinization is proposed based on the needle-like growth of*

72 *metamorphic olivine on primary clinopyroxene, suggesting the presence of serpentine prior to*

73 *the formation of metamorphic olivine. The successive growth of antigorite at the expense of*

74 *both primary and metamorphic olivine constrains the main serpentinization event to*

75 *metamorphic conditions. Finally, a late serpentinization event is proposed based on the*

76 *growth of brucite + antigorite + chrysotile on relict metamorphic. Chr : chromite, P-Ol : primary*

77 *olivine, M-Ol : metamorphic olivine, Opx : primary orthopyroxene, Cpx : primary clinopyroxene,*

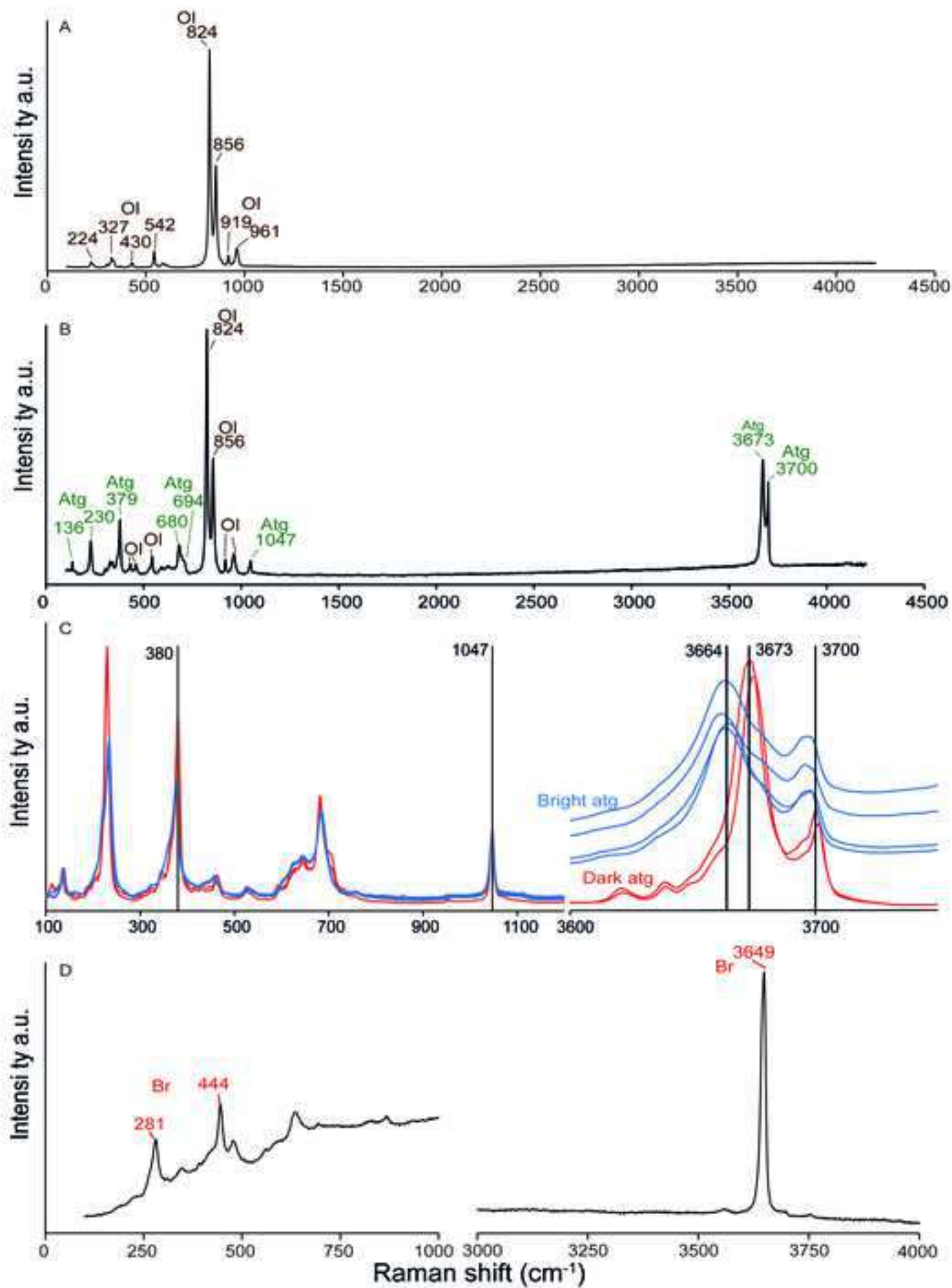78 *Chl : chlorite, Mgt : magnetite, Atg : antigorite, Di : diopside, Brc : brucite, Ctl : chrysotile.*

79 *Fig. 12: Stability field of serpentine type minerals and olivine, modified from Guillot et al.,*

80 *(2015) (see references therein for details on the main reactions). The retrograde P-T path of*

81 *BMC from Honsberger, (2015) is also shown for reference. Atg : antigorite, Brc : brucite; Ctl :*

82 *chrysotile; Ilm : ilmenite; Ol : olivine; Tlc : talc; Ticl : titanian clinohumite.*

Figure 1

Figure 2   Click here to access/download;Figure;Fig2.tif

Figure 3   Click here to access/download;Figure;Fig3.tif ☒

Figure 4
Click here to access/download;Figure;Fig4.tif ±

Figure 6

Figure 7

Figure 8

Figure 8

Figure 9

Figure 10

Click here to access/download;Figure;Fig10.tif

Figure 11   Click here to access/download;Figure;Fig11.tif ⤓

Figure 12
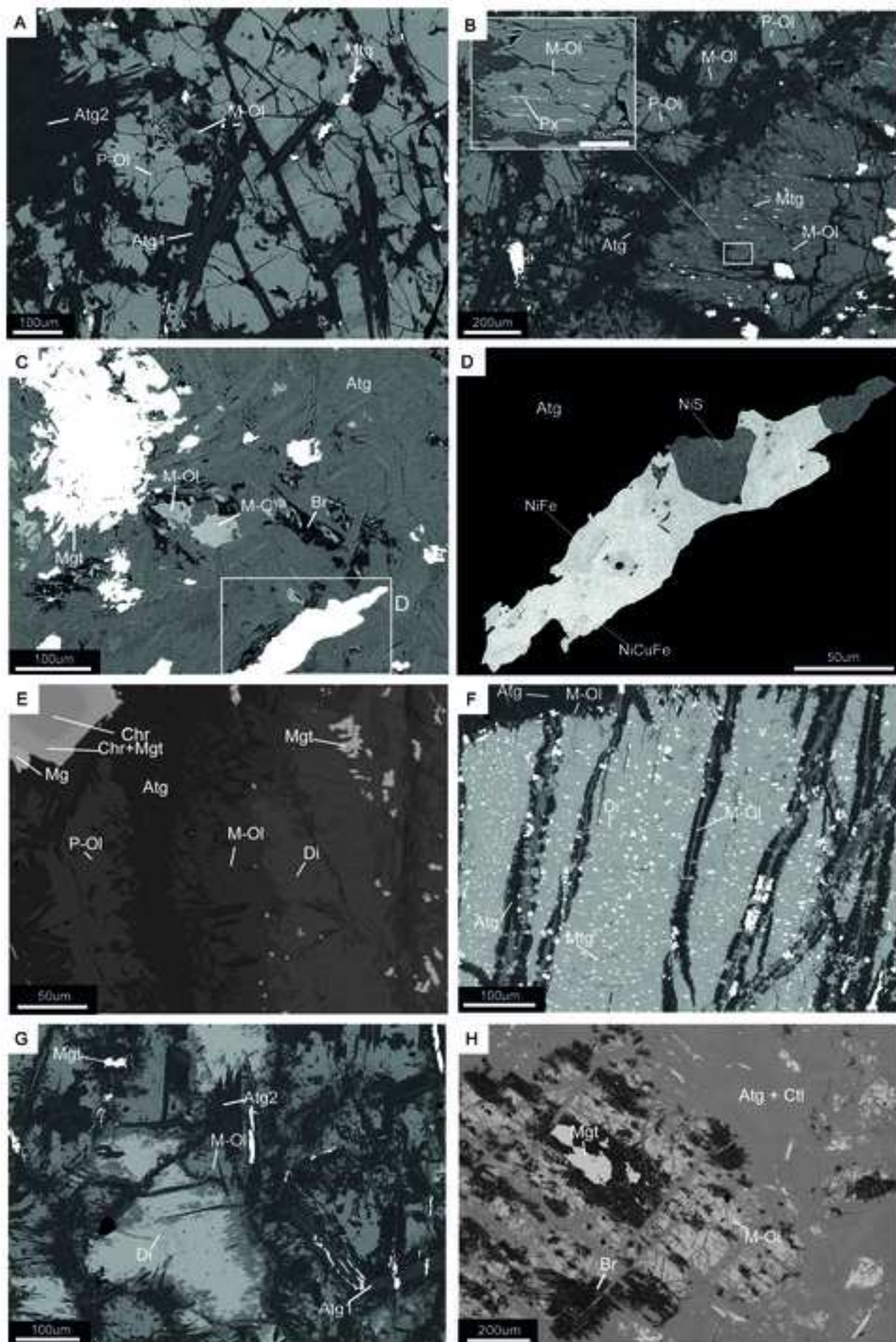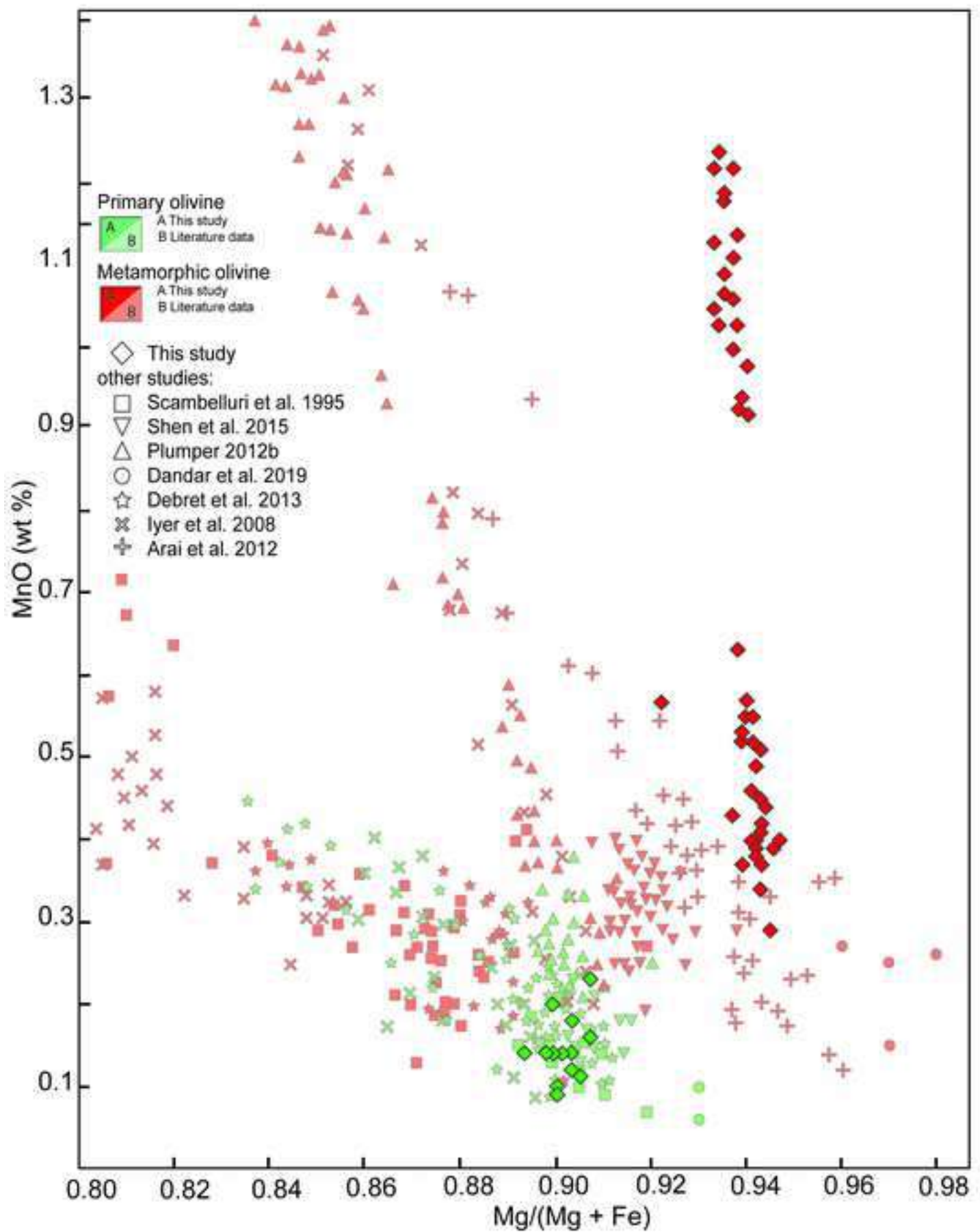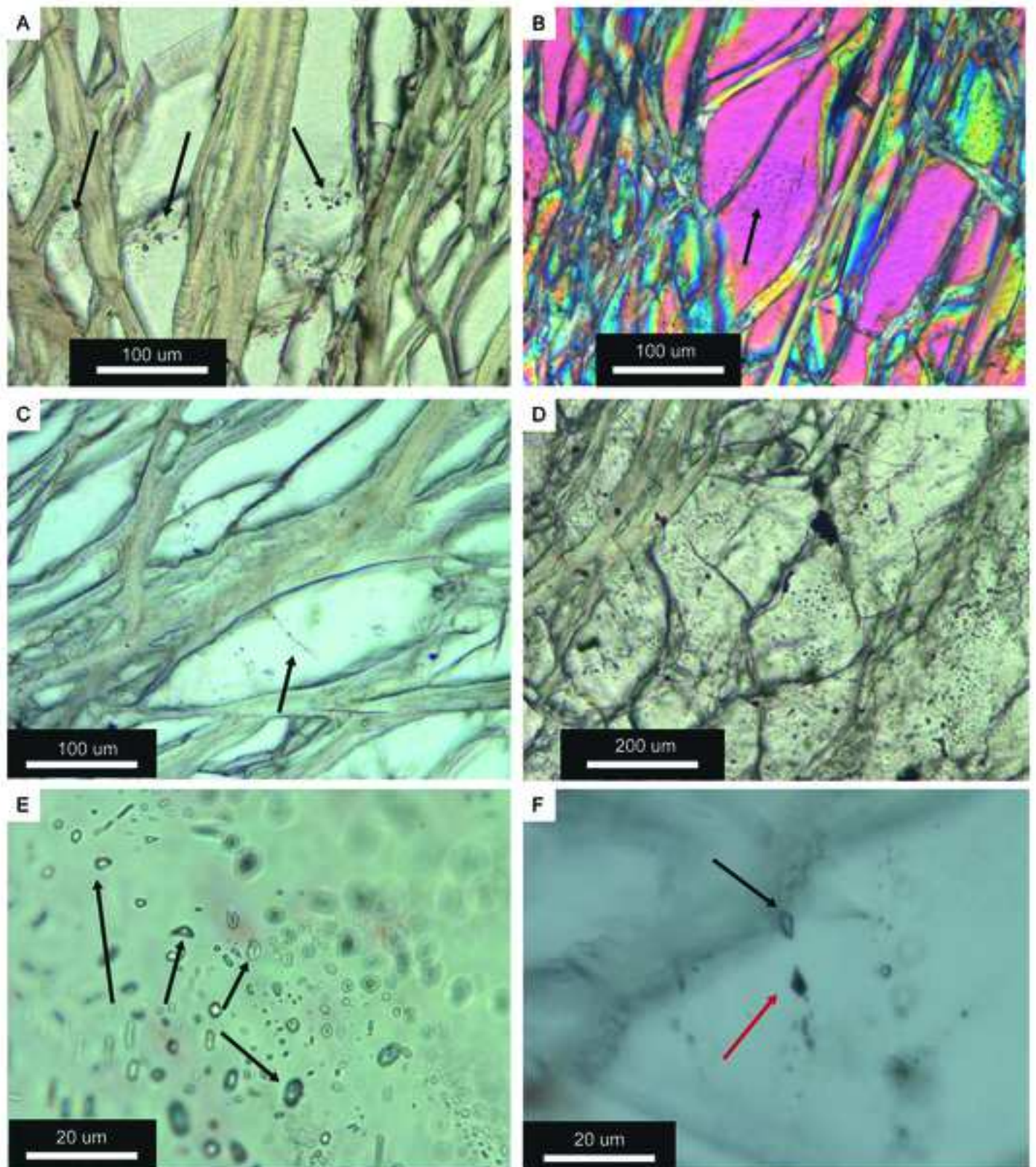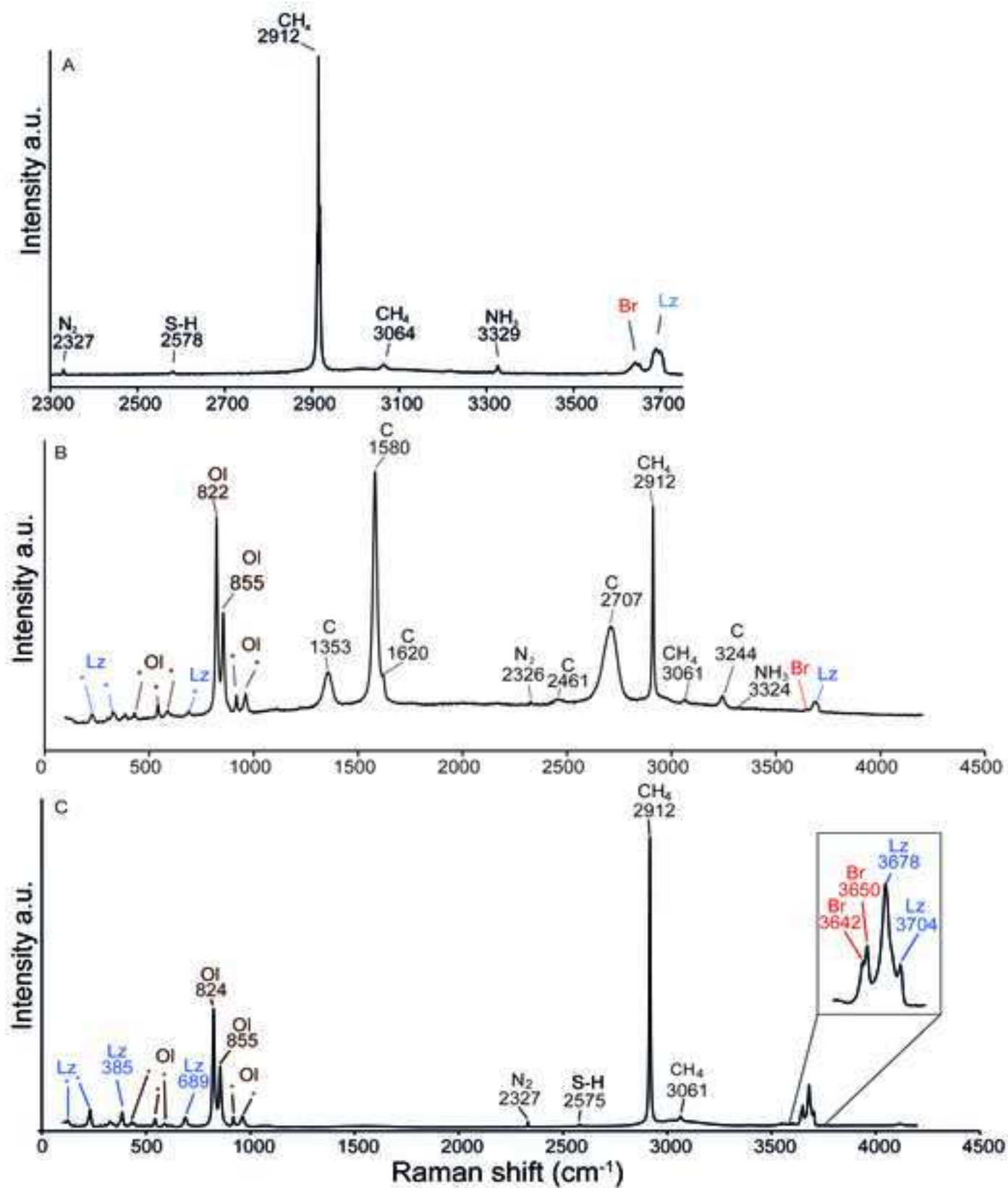
1 **Table 1**

MicroProbe analysis. Absence of SD value when n>1 indicates SD<0.01. *EDS analyses normalized at 100.

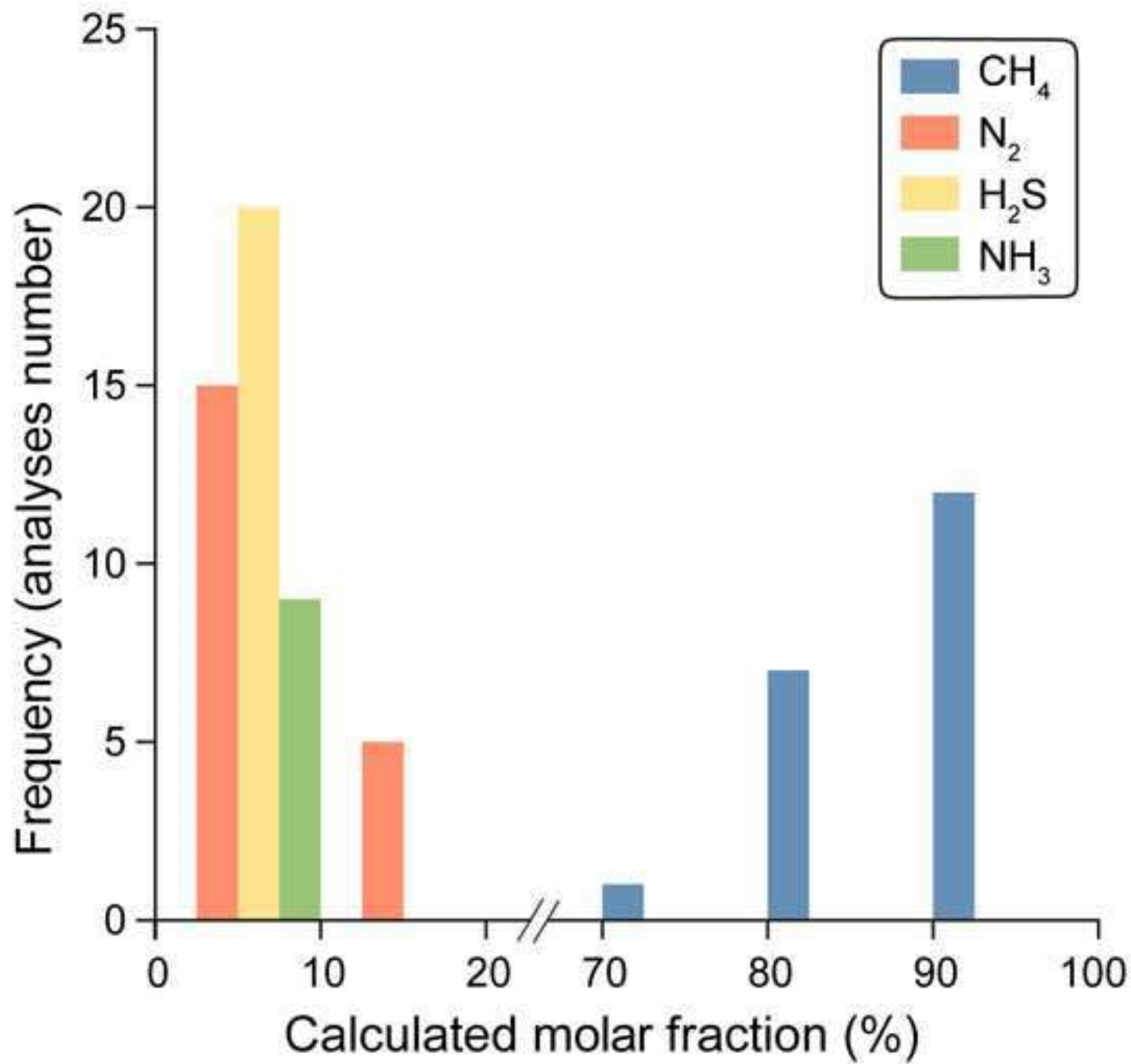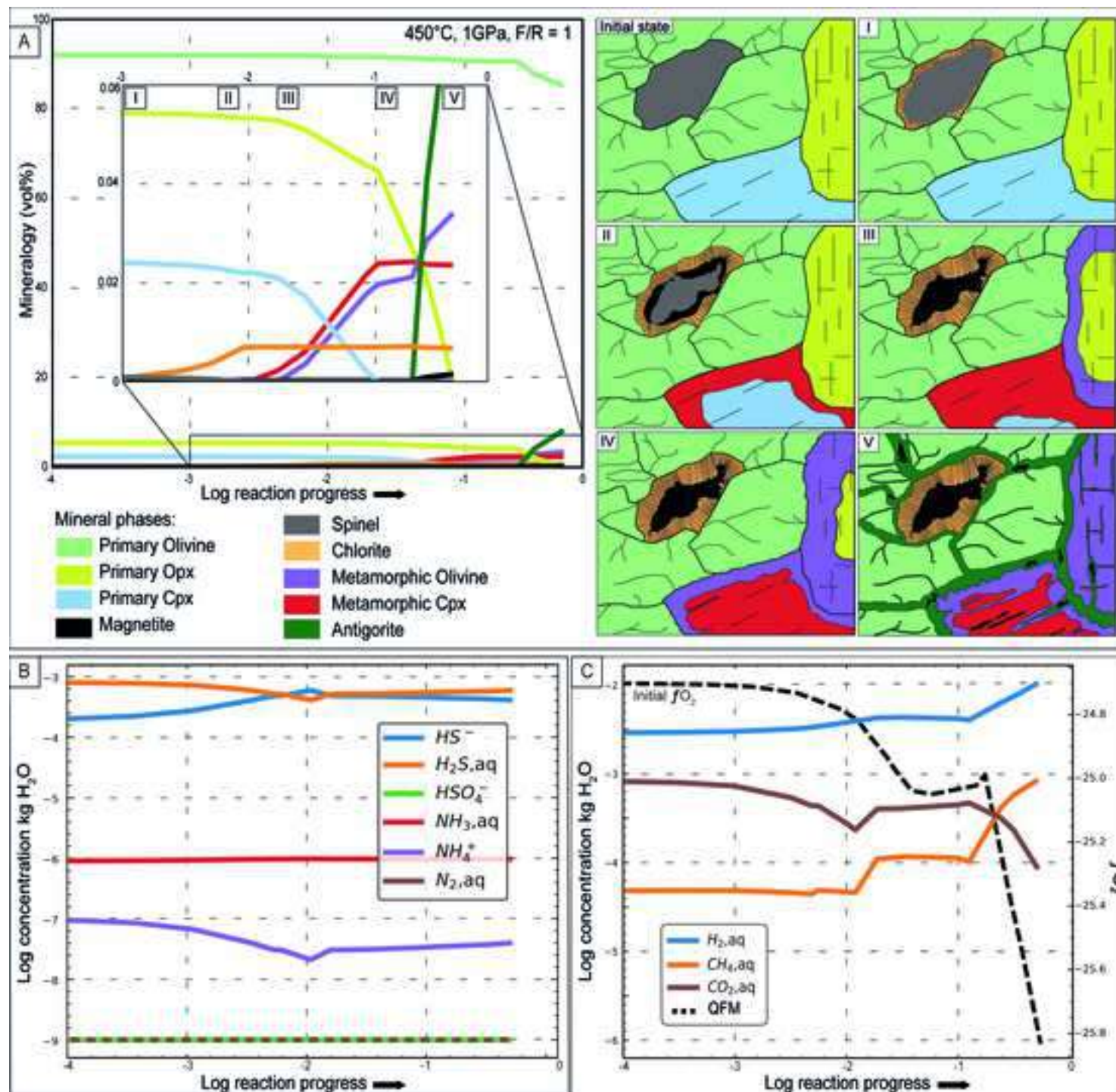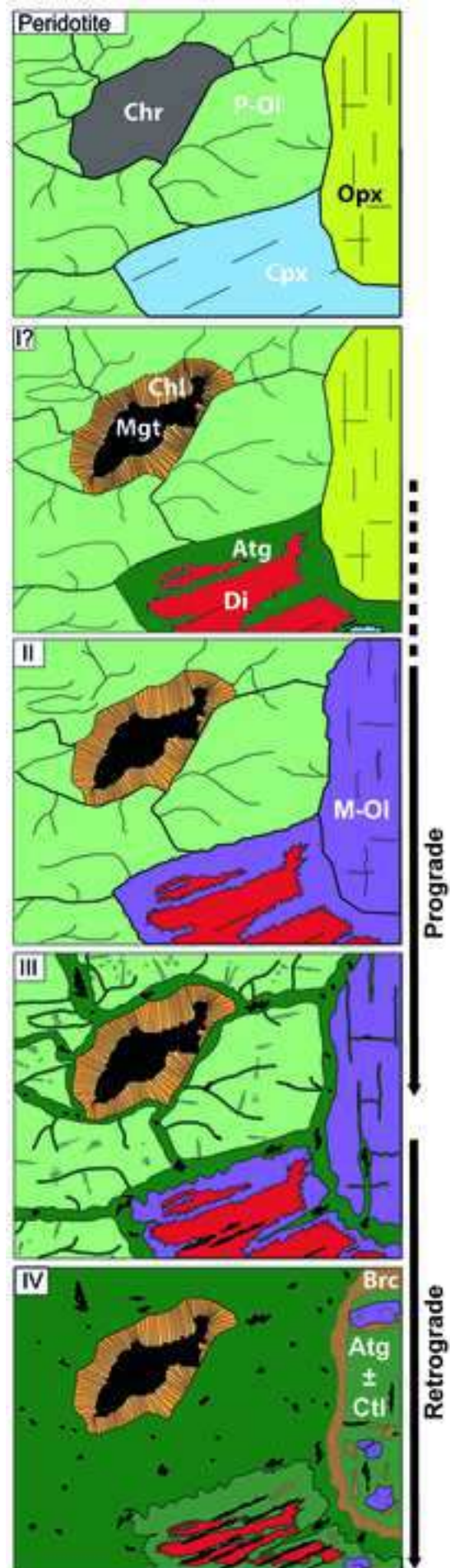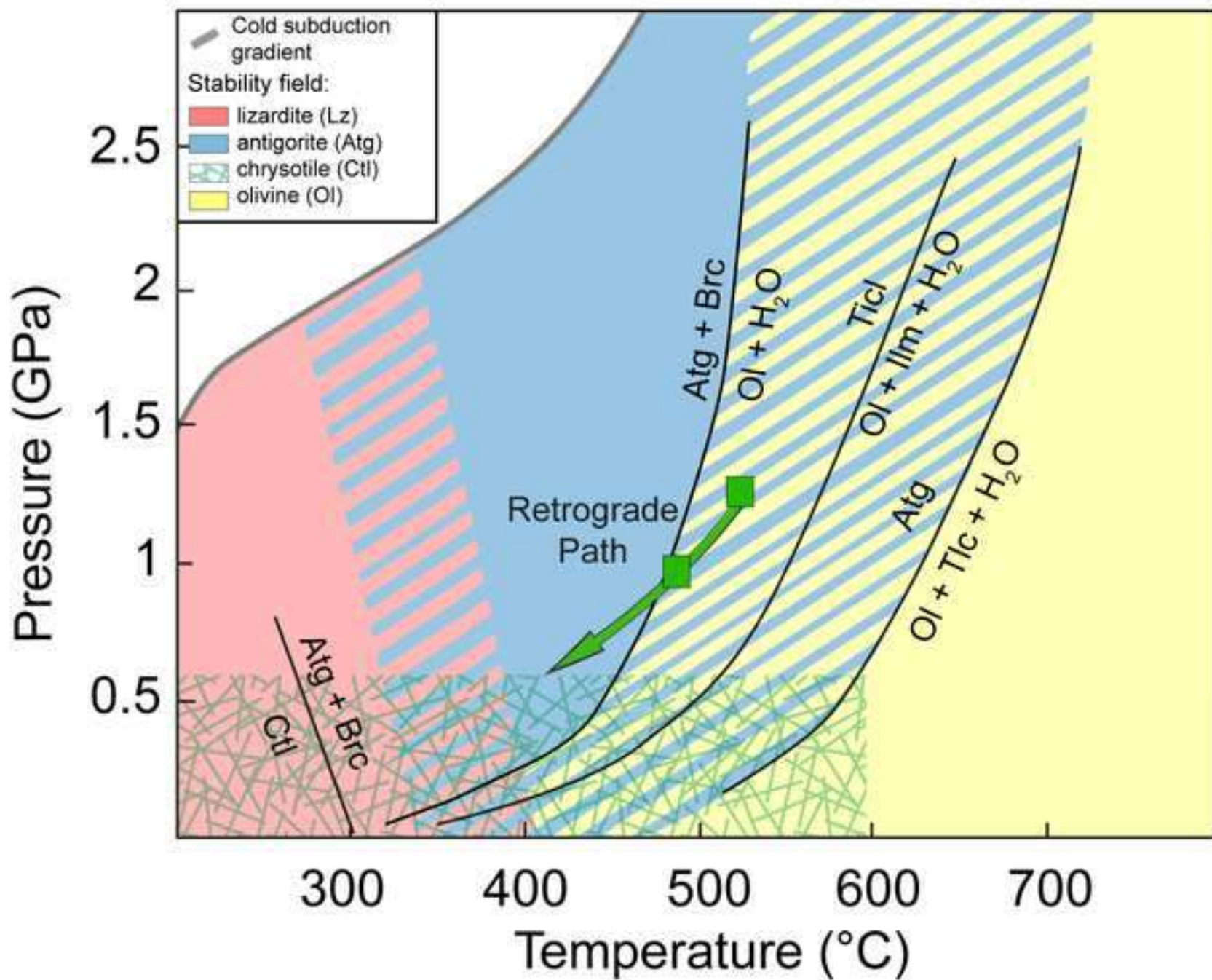| Minerals	Primary Olivine		Metamorphic Olivine			Pyroxene	Serpentine (Bright core)		Serpentine (Matrix)		Chlorite	
Sample	V18-2b	V18-3a	V18-2b	V18-3a	V18-B3*	V18-3a	V18-2b	V18-3a	V18-2b	V18-3a	V18-2b	V18-3a
(n)	14	11	28	15	25	20	6	2	9	4	11	1
SiO_2	40.91 (0.25)	40.83 (0.46)	41.31 (0.49)	41.95 (0.63)	42.00 (0.12)	54.96 (0.98)	42.87 (1.21)	43.41 (0.1)	44.15 (0.17)	43.1 (1.35)	32.61 (1.34)	32.03
TiO_2	0.01 (0.01)	0.02 (0.02)	0.02 (0.01)	0.02 (0.02)		0.03 (0.02)	0.01 (0.01)	0.02 (0.01)	0.02 (0.01)	0 (0)	0.02 (0.02)	0.00
Al_2O_3	0.01 (0.01)	0.01 (0.01)	0.01 (0.02)	0.04 (0.09)		0.15 (0.11)	1.77 (1.22)	1.45 (0.78)	0.52 (0.21)	0.47 (0.26)	14.34 (2.39)	11.78
Cr_2O_3	0.01 (0.02)	0.01 (0.02)	0.06 (0.18)	0.04 (0.03)		0.17 (0.11)	0.61 (0.85)	0.25 (0.19)	0.13 (0.09)	0.1 (0.1)	1.07 (0.56)	4.07
FeO (tot)	8.97 (0.34)	7.93 (0.22)	4.83 (0.30)	5.05 (0.57)	4.71 (0.19)	0.76 (0.16)	2.60 (0.26)	1.58 (0.27)	1.35 (0.22)	1.2 (0.29)	3.31 (0.46)	2.79
MnO	0.15 (0.04)	0.12 (0.06)	0.45 (0.08)	0.37 (0.06)	1.02 (0.18)	0.05 (0.03)	0.04 (0.02)	0.05 (0.05)	0.04 (0.02)	0.02 (0.02)	0.06 (0.10)	0.07
NiO	0.38 (0.03)	0.49 (0.06)	0.43 (0.07)	0.39 (0.06)	0.46 (0.08)	0.03 (0.03)	0.16 (0.02)	0.18 (0.06)	0.15 (0.04)	0.19 (0.02)	0.22 (0.05)	0.24
ZnO	0.04 (0.04)	0.03 (0.04)	0.03 (0.04)	0.03 (0.04)		0.01 (0.02)					0.02 (0.04)	0.00
MgO	50.23 (0.22)	50.91 (0.22)	52.8 (0.64)	51.8 (1.57)	51.80 (0.28)	18.75 (1.15)	37.97 (1.30)	39.81 (0.59)	39.6 (0.77)	40.07 (0.61)	34.34 (1.11)	35.08
CaO	0.02 (0.01)	0.01 (0.02)	0.02 (0.02)	0.25 (0.37)		24.87 (1.43)	0.02 (0.02)	0.05 (0.04)	0.02 (0.02)	0.02 (0.01)	0.02 (0.01)	0.05
Na_2O	0.09 (0.22)	0.01 (0.01)	0.02 (0.02)	0.01 (0.01)		0.04 (0.02)					0.02 (0.03)	0.03
K_2O	0.01 (0.02)	0.01 (0.01)	0.01 (0.01)	0.01 (0.01)		0.01 (0.01)					0.02 (0.02)	0.02
Total,	100.82 (0.36)	100.37 (0.70)	100.06 (1.10)	99.96 (1.63)	100	99.83 (1.12)	86.2 (0.63)	86.93 (0.4)	86.07 (0.82)	85.25 (1.66)	86.14 (0.65)	86.17
Cations												
Si	0.990	0.988	0.991	1.012	1.013	1.989	1.984	2.010	2.044	1.995	6.232	6.165
Ti	0.000	0.000	0.000	0.000		0.001	0.000	0.001	0.001	0.000	0.004	0.000
Al	0.000	0.000	0.000	0.001		0.006	0.091	0.079	0.028	0.026	3.229	2.672
Cr	0.000	0.000	0.001	0.001		0.005	0.026	0.009	0.005	0.004	0.162	0.619
Fe^{2+} (tot)	0.181	0.161	0.097	0.102	0.095	0.023	0.104	0.061	0.052	0.046	0.529	0.404
Mn	0.003	0.003	0.009	0.008	0.021	0.002	0.001	0.002	0.002	0.001	0.010	0.012
Ni	0.007	0.010	0.008	0.008	0.009	0.001	0.006	0.007	0.006	0.007	0.034	0.037
Zn	0.001	0.001	0.000	0.001		0.000					0.003	0.000
Mg	1.812	1.837	1.891	1.861	1.862	1.012	2.486	2.747	2.733	2.765	9.782	10.063
Ca	0.000	0.000	0.001	0.006		0.964	0.001	0.002	0.001	0.001	0.003	0.011
Na	0.004	0.000	0.001	0.000		0.003					0.007	0.012
K	0.000	0.000	0.000	0.000		0.000					0.005	0.005
Mg#	0.91	0.92	0.95	0.95	0.95	0.98	0.94	0.96	0.97	0.97	0.95	0.96

Mg# = Mg/(Mg+ΣFe)

2

3   **Table 2**

MicroProbe analysis. Absence of SD value when n>1 indicates SD<0.01

Minerals	Spinel (nucleus)	Spinel (intermediate)	Magnetite (rim)	Magnetite (mesh and veins)		Brucite
Sample	V18-3a	V18-3a	V18-3a	V18-3a	V18-2b	V18-2b
(n)	7	7	7	1	4	10
SiO_2	0.02 (0.02)	0.03 (0.01)	0.06 (0.07)	0.07	0.05 (0.03)	0.78 (2.20)
TiO_2	0.09 (0.02)	0.23 (0.05)	0.03 (0.02)	0.04	0.01 (0.01)	0.01
Al_2O_3	12.63 (0.94)	3.87 (1.34)	0.00	0.03	0.01 (0.01)	0.01 (0.01)
Cr_2O_3	47.51 (0.57)	41.6 (1.29)	1.87 (1.16)	0.01	0.02 (0.02)	0.04 (0.05)
FeO	34.12 (1.1)	48.32 (2.02)	91.45 (0.75)	92.44	92.57 (0.28)	2.91 (0.18)
MnO	0.34 (0.04)	0.95 (0.36)	0.16 (0.03)	0.12	0.19 (0.05)	0.22 (0.04)
NiO	0.09 (0.02)	0.27 (0.05)	1.05 (0.1)	1.11	0.82 (0.09)	0.38 (0.09)
ZnO	0.49 (0.08)	0.3 (0.1)	0.04 (0.06)	0.10	0.04 (0.08)	0.01 (0.02)
MgO	5.99 (0.32)	3.37 (0.22)	0.71 (0.09)	0.62	0.82 (0.19)	75.88 (3.93)
CaO	0.01 (0.01)	0.00	0 (0.01)	0.00	0.00	0.02 (0.03)
Na_2O	0.03 (0.04)	0.02 (0.02)	0.03 (0.03)	0.03	0.02 (0.04)	0.02 (0.02)
K_2O	0.00	0.01 (0.01)	0 (0.01)	0.01	0.00	0.01 (0.01)
Total	101.4 (0.56)	99.03 (0.6)	95.46 (0.5)	94.63	94.56 (0.45)	80.33 (2.70)
Cr#	0.79(0.01)	0.92(0.2)	1.00			

4   Cr# = Cr/(Al+Cr)

5   **Table 3**

MicroProbe analysis of alloys

Sample	V18-2b						V18-3a		
Alloy	NiFeCu	NiS	NiS	NiS	NiFeCu	NiFeCu	NiS	NiS	NiS
S		24.06	24.25	24.12			24.59	24.52	24.50
Fe	12.21	0.9	0.51	1.35	13.35	20.07	0.84		0.95
Pb				0.13			0.18		
Ni	86.23	72.68	72.71	73.55	86.05	80.03	72.97	72.85	73.30
Cu	1.94				1.75	1.49			
Total:	100.45	97.9	97.59	99.18	101.28	101.71	98.70	97.72	99.04

6   **Table 4**

Calculated partition coefficient between antigorite and olivine for Mg and Mn

	K_D Mg		K_D Mn	
Calculated K_D	V18-2	V18-3b	V18-2	V18-3b
Atg1 / P-Ol	0.25	0.14	0.42	0.54
Atg2 / P-Ol	0.11	0.11	0.42	0.27
Atg1 / M-Ol	0.49	0.23	0.14	0.18
Atg2 / M-Ol	0.21	0.17	0.14	0.09
K_D Atg/Ol from bibliography				
	0.45-0.35		0.18	

K_D Atg/Ol Mg from Evans et al.(2008) and Mn from Trommsdorff and Evans, 1974.